Theoretical and Applied Fracture Mechanics 122 (2022) 103586

Contents lists available at ScienceDirect

Theoretical and Applied Fracture Mechanics

journal homepage: www.elsevier.com/locate/tafmec

A novel analysis of stress intensity factors for distributed non-planar surface cracks and its application to material quality control

Adeyinka Abass [a,b,*], Hisao Matsunaga [c,d,e]

[a] Graduate School of Engineering, Kyushu University, 744 Moto-oka, Nishi-ku, Fukuoka 819-0395, Japan
[b] Konecranes Global Corporation, Koneenkatu 8, Hyvinkää FI-05801, Finland
[c] Department of Mechanical Engineering, Kyushu University, 744 Moto-oka, Nishi-ku, Fukuoka 819-0395, Japan
[d] Research Center for Hydrogen Industrial Use and Storage (HYDROGENIUS), Kyushu University, 744 Moto-oka, Nishi-ku, Fukuoka 819-0395, Japan
[e] International Institute for Carbon-Neutral Energy Research (I2CNER), Kyushu University, 744 Moto-oka, Nishi-ku, Fukuoka 819-0395, Japan

ARTICLE INFO

Keywords:
Stress Intensity Factors
Crack Interaction
Distributed Dislocation Method
Three-Dimensional Crack Analysis
Material Quality Control

ABSTRACT

A novel method for the numerical analysis of stress intensity factors (SIFs) was developed for multiple, 3-D distributed, semi-elliptical cracks on the surface of a semi-infinite elastic body under arbitrary loading conditions. Emphasis was placed on the nature of interactions between cracks, with examination by the distributed infinitesimal dislocation loop technique, an eigenstrain method. SIFs of 100 distributed surface cracks were acquired in approximately 15 min when calculated on a standard personal computer, owing to the numerical integration approaches and meshing procedure adopted. The validity of the obtained results is verified and its applicability to some engineering problems is discussed.

1. Introduction

Prior to the emergence of a dominant major crack, many engineering fracture processes such as corrosion fatigue and fracture of additively-manufactured components can be modelled as a multiple crack problem [1–14]. The computation of the stress intensity factors (SIFs) of the distributed cracks is an essential step in the application of fracture mechanics to practical engineering problems dominated by multiple interacting cracks.

The determination of SIFs of 3-D cracks is a challenging endeavour since it is generally much more intricate, both analytically and numerically, than that of 2-D cracks [15–18]. The presence of a free surface, such as in a semi-infinite body, results in greater difficulty because the free surface constitutes an additional boundary condition that must be considered in the basic formulation of the governing equations [19–29]. Furthermore, when multiple cracks are involved, the computational cost (*e.g.*, analysis time) creates a bottleneck. Although the finite element method (FEM) can be used to calculate the SIFs of 3-D cracks with sufficient accuracy, it is virtually impracticable when multiple distributed small cracks are involved. This is due to the considerable effort required to develop fine meshes in the vicinity of the cracks and the high computational resources necessary to obtain a satisfactory solution [30]. Other numerical approaches such as the body force method (BFM) and boundary integral equation method (BIEM) have found wide applications in 3-D crack analysis [15]. Numerous solutions addressing the case of multiple cracks in an infinite body can be found in the existing literature [31–37]. However, available solutions for multiple cracks in a semi-infinite body remain limited to very unique cases, since the numerical analysis of interacting distributed cracks in an elastic semi-infinite body involves a complicated mathematical formulation. Notwithstanding, the analysis process becomes relatively easier for special cases (*e.g.*, coplanar and parallel cracks).

Murakami employed BFM to study-two dissimilar, semi-elliptical coplanar cracks in a semi-infinite body under tension and bending loading [38,39]. Isida *et al.* also utilised BFM to investigate the interaction of multiple (*i.e.*, two to five), periodically-arrayed, parallel, semi-elliptical surface cracks in a semi-infinite body under tension [40]. Moussa *et al.* used FEM to analyse the nature of the interaction between two identical, non-coplanar, semi-elliptical surface cracks in an infinite plate under tension and pure bending [41]. Åman *et al.* proposed an FEM-based procedure known as the stress component division method (SCDM), to obtain SIFs for interacting arbitrarily-shaped 3-D cracks [42]. SCDM employs commercially-available FEM software for crack interaction analysis without the need for singular elements or complicated meshing procedures. Although SCDM does not require fine meshes in the vicinity of the cracks, it remains computationally expensive when tens or hundreds of randomly-distributed cracks are involved. As

* Corresponding author at: Graduate School of Engineering, Kyushu University, 744 Moto-oka, Nishi-ku, Fukuoka 819-0395, Japan.
E-mail address: abass.adeyinka.073@s.kyushu-u.ac.jp (A. Abass).

https://doi.org/10.1016/j.tafmec.2022.103586
Received 9 September 2022; Accepted 9 September 2022
Available online 22 September 2022

Nomenclature

a	Major radius of a crack
b	Minor radius of a crack
$\vec{b}$	Burgers vector of a dislocation loop
b_x, b_y, b_z	Components of the Burgers vector of a dislocation loop
c	Distance between cracks along the global Z axis
$f_1^{ij}, f_2^{ij}, f_3^{ij}$	Unknown constants of element j of crack i
F_I, F_{II}, F_{III}	Dimensionless Modes I, II and III stress intensity factors
h	Distance between cracks along the global X axis
K_{ij}	Kernel function of the fundamental infinitesimal dislocation solution
K_I, K_{II}, K_{III}	Modes I, II, III stress intensity factors
l, m, n	Local crack coordinate system
N	Total number of cracks in the body
X, Y, Z	Global coordinate system
$T_{jkm}(\boldsymbol{x}, \boldsymbol{\xi})$	Stress tensor at point $\boldsymbol{x}$ due to unit point forces at $\boldsymbol{\xi}$ in a semi-infinite body
x, y, z	Coordinate system of point $\boldsymbol{x}$
α	A parameter that can take the value of 0, 0.5 or 1.0
$\gamma_A, \gamma_B, \gamma_C$	Interaction factor at points A, B and C
δ_{ij}	Kronecker delta
δS	Area of an infinitesimal dislocation loop
μ	Modulus of rigidity
ν	Poisson's ratio
$\sigma_{iz}(\boldsymbol{x})$	Stress components at point $\boldsymbol{x}$ of the semi-infinite body
ξ, η, ζ	Coordinate system of point $\boldsymbol{\xi}$
FEM	Finite element method
IDL	Infinitesimal dislocation loop
SCDM	Stress component division method
BFM	Body force method
BIEM	Boundary integral equation method
SIF	Stress Intensity Factor

previously noted, the existing literature reflects a dearth of analysis for arbitrarily-distributed cracks in a semi-infinite body under tension and shear loading. Therefore, further development of analysis methods is expected to more precisely tackle problems where the fracture process is dominated by nucleation, interaction and coalescence of randomly-distributed cracks.

This study advances the numerical analysis of SIFs for multiple non-planar, semi-elliptical cracks that were distributed on the surface of a semi-infinite elastic body under arbitrary loading conditions. The eigenstrain method adopted for the investigation is based on the technique of distributing infinitesimal dislocation loops (IDLs) on the crack surfaces in order to satisfy their respective boundary conditions [43–46]. This formulation led to a set of 2-D, hyper-singular integral equations. The integral equations had a singularity of order three and were interpreted in the Hadamard finite-part sense [46,47]. In the numerical calculation, the crack regions were discretized into triangular sections. The discretization transformed the integral equations into a system of algebraic equations which were then solved *via* the inverse method. The nature of the interaction among cracks was studied with some examples. Moreover, applications of the developed method to practical problems, such as corrosion fatigue and material quality control, will be discussed.

2. Basic formulation

At first, a semi-infinite elastic body was considered under arbitrary loading conditions with no cracks. It was assumed that the stress state at every point of the body was known based on a suitable analytical or numerical method. Multiple, distributed, non-planar, semi-elliptical cracks were then introduced on the surface of the body, as shown in Fig. 1. Each crack possessed its own local coordinate system, as can be seen in Fig. 2. Since the origin of each local coordinate system could be expressed in the global coordinate system, they were mutually transformable. In general, the crack-faces can undergo three displacement modes as a result of the external boundary conditions: opening mode (Mode I), shearing mode (Mode II) and tearing mode (Mode III). The central aim of this research was to determine the distribution functions of the relative displacement of crack-faces in each crack. Once the displacement functions are identified, SIFs corresponding to the three modes can easily be ascertained from the asymptotic relationship between crack-front displacement discontinuities and SIFs [44].

When the cracks are modelled as continuously-distributed IDLs with the area of an IDL, δS, and Burgers vector, $\vec{b} = (b_x, b_y, b_z)$, the relative displacements of the crack-faces are represented by $\vec{b}$ of the IDLs [48].

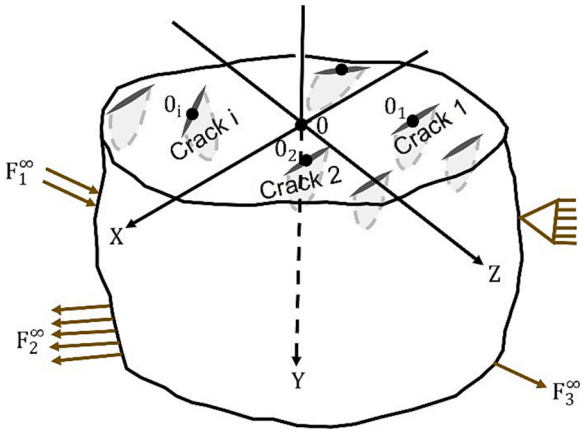

Fig. 1. Distribution of cracks on the surface of a semi-infinite body under arbitrary loading conditions.

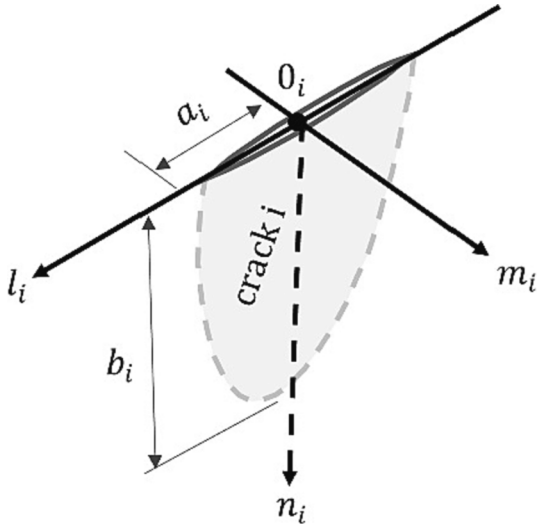

Fig. 2. Local crack coordinate system.

Therefore, once the Burgers vector components are obtained for each crack, the three relative displacement modes of the crack-faces can be determined. Following the coordinate system in Fig. 2, the Mode I displacement corresponds to b_z, while b_x and b_y correspond to displacements in Modes II and III, respectively. The correct distributions of the IDLs are those which satisfy the traction-free condition on overall crack-faces. This formulation resulted in a set of 2-D, hyper-singular integral equations. In order to derive the integral equations, it was necessary to obtain the expressions for the stresses at any point in a semi-infinite body due to an IDL at an arbitrary location in the body. In Fig. 3, of interest were the stress components, $\sigma_{iz}(\boldsymbol{x})$, at point $\boldsymbol{x}$, due to an IDL of area and location at point $\boldsymbol{\xi}$. $\sigma_{iz}(\boldsymbol{x})$ is expressed by:

$$\sigma_{iz}(\boldsymbol{x}) = K_{ij}(\boldsymbol{x},\boldsymbol{\xi})b_j(\boldsymbol{\xi}) \tag{1}$$

where,

$i,j: x, y$ and z;

$\sigma_{iz}(\boldsymbol{x})$ are stress components at point $\times$in the semi-infinite body expressed in the local coordinate system of the crack where $\boldsymbol{x}$ is located.

$b_j(\boldsymbol{\xi})$ are components of the Burgers vector of the IDL at point $\boldsymbol{\xi}$ expressed in the local coordinate system of the crack where $\boldsymbol{\xi}$ is located; and.

$K_{ij}(\boldsymbol{x},\boldsymbol{\xi})$ denotes Kernel function, the fundamental infinitesimal dislocation solution.

The expression for $K_{ij}(\boldsymbol{x},\boldsymbol{\xi})$ was derived in tensor form by Bacon and Groves [49] as:

$$K_{ij}(\boldsymbol{x},\boldsymbol{\xi}) = \mu\left[\frac{\partial T_{ziz}(\boldsymbol{x},\boldsymbol{\xi})}{\partial \boldsymbol{\xi}_j} + \frac{\partial T_{zij}(\boldsymbol{x},\boldsymbol{\xi})}{\partial \zeta} + \frac{2\nu}{1-2\nu}\frac{\partial T_{zim}(\boldsymbol{x},\boldsymbol{\xi})}{\partial \boldsymbol{\xi}_m}\delta_{ij}\right] \tag{2}$$

where,

$T_{jkm}(\boldsymbol{x},\boldsymbol{\xi})$ is the stress tensor at point $\boldsymbol{x}(x,y,z)$ due to unit point forces at $\boldsymbol{\xi}(\xi,\eta,\zeta)$ in a semi-infinite body, as first derived by Mindlin [50];

μ is Modulus of rigidity;

ν is Poisson's ratio;

x, y, z represents the coordinate system of point $\boldsymbol{x}$;

ξ,η,ζ denotes the coordinate system of point $\boldsymbol{\xi}$; and.

δ_{ij} is Kronecker delta.

Starting from the Mindlin solution for stresses in a semi-infinite body due to three unit point forces, P, Q and R, pointing in the z, x and y axes, respectively, the explicit expression of Eq. (1) is given as follows:

$$\begin{aligned}\sigma_{zz} = {} & \frac{2\mu(1-\nu)}{1-2\nu}\left[\frac{\partial\sigma^{P}_{zz}}{\partial\zeta} + \frac{\nu}{1-\nu}\left(\frac{\partial\sigma^{Q}_{zz}}{\partial\xi} + \frac{\partial\sigma^{R}_{zz}}{\partial\eta}\right)\right]b_z \\ & + \mu\left[\frac{\partial\sigma^{P}_{zz}}{\partial\xi} + \frac{\partial\sigma^{Q}_{zz}}{\partial\zeta}\right]b_x + \mu\left[\frac{\partial\sigma^{P}_{zz}}{\partial\eta} + \frac{\partial\sigma^{R}_{zz}}{\partial\zeta}\right]b_y\end{aligned} \tag{3a}$$

$$\begin{aligned}\tau_{xz} = {} & \frac{2\mu(1-\nu)}{1-2\nu}\left[\frac{\partial\tau^{P}_{xz}}{\partial\zeta} + \frac{\nu}{1-\nu}\left(\frac{\partial\tau^{Q}_{xz}}{\partial\xi} + \frac{\partial\tau^{R}_{xz}}{\partial\eta}\right)\right]b_z \\ & + \mu\left[\frac{\partial\tau^{P}_{xz}}{\partial\xi} + \frac{\partial\tau^{Q}_{xz}}{\partial\zeta}\right]b_x + \mu\left[\frac{\partial\tau^{P}_{xz}}{\partial\eta} + \frac{\partial\tau^{R}_{xz}}{\partial\zeta}\right]b_y\end{aligned} \tag{3b}$$

$$\begin{aligned}\tau_{yz} = {} & \frac{2\mu(1-\nu)}{1-2\nu}\left[\frac{\partial\tau^{P}_{yz}}{\partial\zeta} + \frac{\nu}{1-\nu}\left(\frac{\partial\tau^{Q}_{yz}}{\partial\xi} + \frac{\partial\tau^{R}_{yz}}{\partial\eta}\right)\right]b_z \\ & + \mu\left[\frac{\partial\tau^{P}_{yz}}{\partial\xi} + \frac{\partial\tau^{Q}_{yz}}{\partial\zeta}\right]b_x + \mu\left[\frac{\partial\tau^{P}_{yz}}{\partial\eta} + \frac{\partial\tau^{R}_{yz}}{\partial\zeta}\right]b_y\end{aligned} \tag{3c}$$

An investigation of the genesis of Eq. (3) required 21 painstaking derivatives of expressions for the stress components in the Mindlin solution, undertaken for the first time for the present study and provided in detail in Appendix A.

With the solution of stresses at a given point courtesy of an arbitrarily-located IDL now available, the formulation of an integral equation system becomes straightforward. The total number of surface cracks should be N under arbitrary loading conditions, where the crack-faces undergo three modes of relative displacement. These relative displacements were modelled as distributed IDL, $\vec{b}$, the distribution function of which was unknown for each crack. The correct density distribution of the IDLs for each crack simultaneously satisfied the traction-free conditions on overall crack-faces. In other words, the correct distribution was that which nullified the stresses due to external loadings at locations occupied by the cracks. Mathematically, this condition is expressed by:

$$\sum_{k=1}^{N}\left(\int_{S_k} K_{ij}(\boldsymbol{x},\boldsymbol{\xi})b^{k}_{j}(\boldsymbol{\xi})\delta S\right) = -t^{\infty}_{i}(\boldsymbol{x}) \tag{4}$$

where,

$t^{\infty}_{i} = \begin{bmatrix}\sigma^{\infty}_{xz}\\ \sigma^{\infty}_{yz}\\ \sigma^{\infty}_{zz}\end{bmatrix}$ are stresses at point $\boldsymbol{x}$ due to external loading;

N represents the total number of cracks in the body;

$b^{k}_{j}(\boldsymbol{\xi})$ is the Burgers vector component of the IDL at point $\boldsymbol{\xi}$ of the k_{th} crack; and.

S_k is the integration area of the k_{th} crack.

The unknown terms in the set of integral equations were the distribution densities of b^{k}_{j} for the cracks, the solutions of which can be applied to compute many fracture mechanics parameters of practical importance. In this case, they were adopted to compute the SIFs for the cracks using the asymptotic relationship.

Since it was not possible to derive an analytical solution for the set of

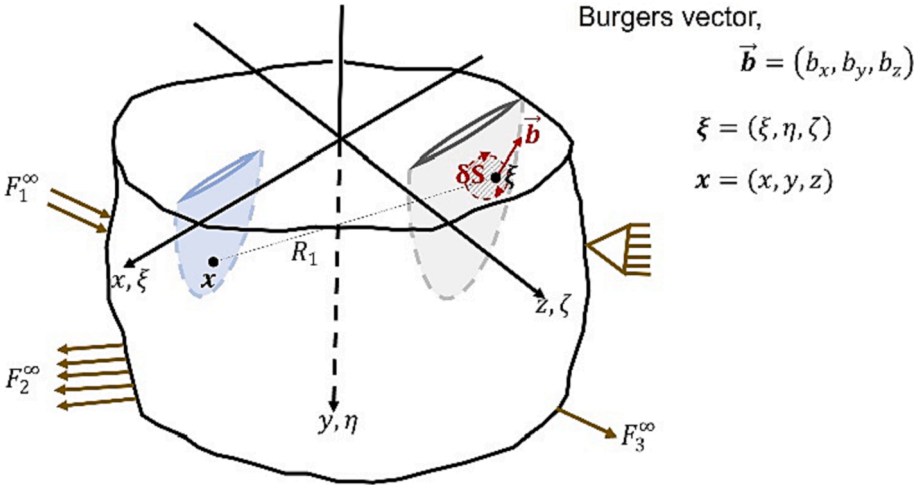

Fig. 3. Stresses in a semi-infinite body due to an infinitesimal dislocation loop.

integral equations in Eq. (4), a numerical procedure was therefore required. Furthermore, Eq. (4) comprises a set of hyper-singular integral equations because $K_{ij}(\boldsymbol{x},\boldsymbol{\xi})$ has a singularity of order 3 as $\boldsymbol{x}$ approaches $\boldsymbol{\xi}$. This can be confirmed by a review of the equations in Appendix A. Hence, Eq. (4) must be interpreted in the Hadamard finite-part sense [47].

3. Numerical procedure

It is noteworthy that the preceding formulation and derived equations were independent of the geometry of the cracks. In this case, the following numerical procedures were developed specifically for arbitrarily-distributed surface cracks, all of which were semi-elliptical in shape with different aspect ratios. Each crack-plane was divided into a few triangular segments, following the simple pattern featured in Fig. 4. The unknown field function was represented as a piecewise constant approximation, whereby it was approximated by the product of a known weight function and an unknown constant. The choice of the weight function is important for the effectiveness and accuracy of the approximation. In the case of elliptical cracks, an analytical expression for a suitable weight function was proposed by Eshelby [44]. Therefore, the relative crack-face displacement function, $\overrightarrow{\boldsymbol{b}} = (b_x, b_y, b_z)$, for the j_{th} element in the i_{th} crack is approximated numerically by:

$$b_x^{i,j} = \left(1-\frac{x^2}{a_i^2}-\frac{y^2}{b_i^2}\right)^{1/2} f_1^{i,j};\ b_y^{i,j} = \left(1-\frac{x^2}{a_i^2}-\frac{y^2}{b_i^2}\right)^{1/2} f_2^{i,j};\ b_z^{i,j} = \left(1-\frac{x^2}{a_i^2}-\frac{y^2}{b_i^2}\right)^{1/2} f_3^{i,j} \tag{5}$$

where,

$b_x^{i,j}$, $b_y^{i,j}$, $b_z^{i,j}$ are components of the Burgers vector of the j_{th} element in the i_{th} crack;

a_i, b_i are the major and minor radii of the i_{th} crack; and.

$f_1^{i,j}$, $f_2^{i,j}$, $f_3^{i,j}$ are constants of the j_{th} element in the i_{th} crack.

Furthermore, the traction-free requirement on overall crack-faces is relaxed, such that it is only enforced at the centroid of the elements [20,22,38,44]. Therefore, Eq. (4) can be rewritten as:

$$\sum_{m=1}^{N_e}\left(K_{mn}^{33}f_3^m + K_{mn}^{32}f_2^m + K_{mn}^{31}f_1^m\right) = -\sigma_{zz\infty}^n(x^n,y^n)(n=1,2,\cdots,N_e) \tag{6a}$$

$$\sum_{m=1}^{N_e}\left(K_{mn}^{23}f_3^m + K_{mn}^{22}f_2^m + K_{mn}^{21}f_1^m\right) = -\sigma_{yz\infty}^n(x^n,y^n)(n=1,2,\cdots,N_e) \tag{6b}$$

$$\sum_{m=1}^{N_e}\left(K_{mn}^{13}f_3^m + K_{mn}^{12}f_2^m + K_{mn}^{11}f_1^m\right) = -\sigma_{xz\infty}^n(x^n,y^n)(n=1,2,\cdots,N_e) \tag{6c}$$

Equation (6), in turn, can then be revised in matrix format, as documented in Eq. (7).

$$\sum_{m=1}^{N_e}\left(\begin{bmatrix} K_{mn}^{33} & K_{mn}^{32} & K_{mn}^{31} \\ K_{mn}^{23} & K_{mn}^{22} & K_{mn}^{21} \\ K_{mn}^{13} & K_{mn}^{12} & K_{mn}^{11} \end{bmatrix} \bullet \begin{bmatrix} f_3^m \\ f_2^m \\ f_1^m \end{bmatrix}\right) = \begin{bmatrix} -\sigma_{zz\infty}^n(x^n,y^n) \\ -\sigma_{yz\infty}^n(x^n,y^n) \\ -\sigma_{xz\infty}^n(x^n,y^n) \end{bmatrix} (n=1,2,\cdots,N_e) \tag{7}$$

where,

N_e is the total number of elements;

(x^n, y^n) are the centroid coordinates of the n_{th} element; and.

$\sigma_{xz\infty}^n$, $\sigma_{yz\infty}^n$ and $\sigma_{zz\infty}^n$ are stresses at the centroid of the n_{th} element.

Expressions for the Kernel matrix in Eq. (7) can be obtained *via* multiplication of Eq. (3) by the weighing function, as presented in Table 1, where a_m and b_m are the major and minor radii of the crack to which the m_{th} element belongs. The derivatives in their complete format

Table 1
Expressions for the Kernel matrix of Eq. (7).

Kernel	Expression
K_{mn}^{11}	$\mu\left[\frac{\partial\tau_{xz}^P}{\partial\xi}+\frac{\partial\tau_{xz}^Q}{\partial\zeta}\right]\left(1-\frac{x^2}{a_m^2}-\frac{y^2}{b_m^2}\right)^{1/2}$
K_{mn}^{12}	$\mu\left[\frac{\partial\tau_{xz}^P}{\partial\eta}+\frac{\partial\tau_{xz}^R}{\partial\zeta}\right]\left(1-\frac{x^2}{a_m^2}-\frac{y^2}{b_m^2}\right)^{1/2}$
K_{mn}^{13}	$\frac{2\mu(1-\nu)}{1-2\nu}\left[\frac{\partial\tau_{xz}^P}{\partial\zeta}+\frac{\nu}{1-\nu}\left(\frac{\partial\tau_{xz}^Q}{\partial\xi}+\frac{\partial\tau_{xz}^R}{\partial\eta}\right)\right]\left(1-\frac{x^2}{a_m^2}-\frac{y^2}{b_m^2}\right)^{1/2}$
K_{mn}^{21}	$\mu\left[\frac{\partial\tau_{yz}^P}{\partial\xi}+\frac{\partial\tau_{yz}^Q}{\partial\zeta}\right]\left(1-\frac{x^2}{a_m^2}-\frac{y^2}{b_m^2}\right)^{1/2}$
K_{mn}^{22}	$\mu\left[\frac{\partial\tau_{yz}^P}{\partial\eta}+\frac{\partial\tau_{yz}^R}{\partial\zeta}\right]\left(1-\frac{x^2}{a_m^2}-\frac{y^2}{b_m^2}\right)^{1/2}$
K_{mn}^{23}	$\frac{2\mu(1-\nu)}{1-2\nu}\left[\frac{\partial\tau_{yz}^P}{\partial\zeta}+\frac{\nu}{1-\nu}\left(\frac{\partial\tau_{yz}^Q}{\partial\xi}+\frac{\partial\tau_{yz}^R}{\partial\eta}\right)\right]\left(1-\frac{x^2}{a_m^2}-\frac{y^2}{b_m^2}\right)^{1/2}$
K_{mn}^{31}	$\mu\left[\frac{\partial\sigma_{zz}^P}{\partial\xi}+\frac{\partial\sigma_{zz}^Q}{\partial\zeta}\right]\left(1-\frac{x^2}{a_m^2}-\frac{y^2}{b_m^2}\right)^{1/2}$
K_{mn}^{32}	$\mu\left[\frac{\partial\sigma_{zz}^P}{\partial\eta}+\frac{\partial\sigma_{zz}^R}{\partial\zeta}\right]\left(1-\frac{x^2}{a_m^2}-\frac{y^2}{b_m^2}\right)^{1/2}$
K_{mn}^{33}	$\frac{2\mu(1-\nu)}{1-2\nu}\left[\frac{\partial\sigma_{zz}^P}{\partial\zeta}+\frac{\nu}{1-\nu}\left(\frac{\partial\sigma_{zz}^Q}{\partial\xi}+\frac{\partial\sigma_{zz}^R}{\partial\eta}\right)\right]\left(1-\frac{x^2}{a_m^2}-\frac{y^2}{b_m^2}\right)^{1/2}$

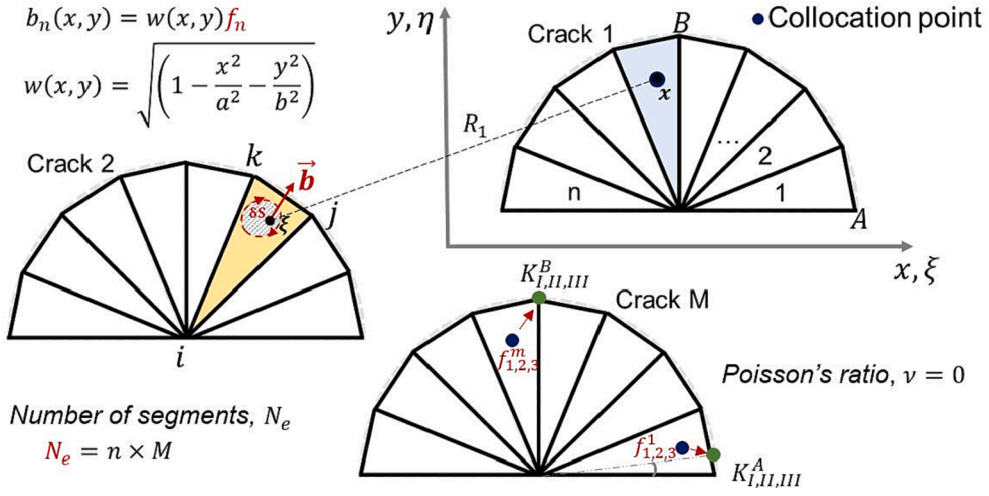

Fig. 4. Discretization of the crack-faces into triangular segments.

are provided in Appendix A.

In addition, evaluation of the kernels requires the numerical integration of the expressions over the element where the IDLs are distributed. In cases where the evaluation point (x^n, y^n) lies outside of the integration area (*i.e.*, $n \neq m$), a conventional 2-D quadrature approach can be employed. On the other hand, in cases where $n = m$, such a technique is not applicable due to the presence of terms with third order singularity, for which any special procedure would be needed. In this study, the method proposed by Dai *et al.* [45] was adopted and successfully implemented. The sequence of equations in Eq. (7) can be solved using a standard solution routine to determine the unknown constants. The relative crack-face displacements for each element can be deduced using Eq. (5). Moreover, the SIFs for a target crack-front point can be established using the asymptotic relationship between relative crack-face displacement and SIFs. For elliptical cracks, dimensionless SIFs (F_{I}, F_{II}, F_{III}) at a point $p\left(x_{\mathrm{p}}, y_{\mathrm{p}}\right)$ along the crack-front can be determined by Eq. (8). Prior to using Eq. (8), f_{n} and f_{t} at point p, corresponding to the displacement discontinuities along the lines normal and tangential to the crack-front, should be evaluated using the equivalent values of f_1 and f_2, as well as a suitable vector transformation rule.

$$F_{\mathrm{I}}^{\mathrm{p}} = \frac{2\pi f_3^{\mathrm{p}}}{b}\left(\sin^2\beta + \frac{b^2}{a^2}\cos^2\beta\right)^{1/4} \tag{8a}$$

$$F_{\mathrm{II}}^{\mathrm{p}} = \frac{2\pi f_{\mathrm{n}}^{\mathrm{p}}}{b}\left(\sin^2\beta + \frac{b^2}{a^2}\cos^2\beta\right)^{1/4} \tag{8b}$$

$$F_{\mathrm{III}}^{\mathrm{p}} = \frac{2\pi f_{\mathrm{t}}^{\mathrm{p}}}{b}\left(\sin^2\beta + \frac{b^2}{a^2}\cos^2\beta\right)^{1/4} \tag{8c}$$

where,

$\tan\beta = \frac{a y_{\mathrm{p}}}{b x_{\mathrm{p}}}$; and.

$$F_{\mathrm{I}}^{\mathrm{p}} = \frac{K_{\mathrm{I}}^{\mathrm{p}}}{\sigma_\infty\sqrt{\pi b}} \;;\; F_{\mathrm{II}}^{\mathrm{p}} = \frac{K_{\mathrm{II}}^{\mathrm{p}}}{\tau_\infty\sqrt{\pi b}} \;;\; F_{\mathrm{III}}^{\mathrm{p}} = \frac{K_{\mathrm{III}}^{\mathrm{p}}}{\tau_\infty\sqrt{\pi b}}$$

4. Numerical results and discussion

In this section, the afore-mentioned procedures are applied to some problems of practical importance. In all cases, each crack was divided into nine segments, based on the pattern showcased in Fig. 4. This pattern and the number of divisions, obtained by trial and error, provided the best compromise between analysis time and accuracy. Analysis for one crack took about 5 s on average when performed on a typical desktop computer with prevalent CPU (*e.g.*, Intel(R) Core (TM) i3-8100 CPU 3.60 GHz), *i.e.*, for n number of cracks, the analysis took approximately $(n \times 5)$ s. A significant portion of the analysis time was used in the determination of the Kernel matrix in Eq. (7).

Poisson's ratio, ν, was set to zero in all cases because the other values ($\nu \neq 0$) led to an increase of approximately 1 s per crack in the analysis, while the change in the SIFs was minor, *i.e.*, the difference was primarily within a 5 % range. Therefore, it was concluded that since the effect of Poisson's ratio was small, it could be set to zero to save research time. Several studies on the stress singularity at/near a corner point (*i.e.*, a point where the crack-front intersects with the free surface) reported the effect of Poisson's ratio on the nature of singularity [23,24,26,27,45,46]. However, since such exceptional singularity behaviour at the corner point does not exist when $\nu = 0$, the stress singularity remains at $r^{-0.5}$ [26].

As will be demonstrated by the example of a semi-elliptical surface crack under tension, the accuracy of the analysis results for the proposed method is comparable to that of earlier works. In the following, the method's precision is first established for a semi-elliptical surface crack with various aspect ratios under tension. Subsequently, more complex examples will be analysed (*e.g.*, parallel arrays of surface cracks and randomly-distributed surface cracks under tension) and some interesting observations will be discussed.

4.1. Single semi-elliptical surface crack under tension

Fig. 5 portrays a single semi-elliptical surface crack under remote tension. In this case, Mode I SIFs, K_{IA}, near the corner point at free surface A, and K_{IB}, at the deepest point B, were analysed, where the crack aspect ratio, b/a, ranged from 0.1 to 10. The obtained dimensionless SIFs are listed in Table 2 and presented in Fig. 6. Where available, the values acquired by Murakami [21] are attached in parentheses for comparison purposes. In Murakami's analysis, Poisson's ratio was 0.3, while in this study it was set to zero, a factor which may explain the difference between the results. Nevertheless, the variance was always less than 3 %. The result indicates that the accuracy of this method is sufficient for practical applications.

4.2. Parallel semi-elliptical surface cracks under tension

Due to the complexity of the problem, the analysis of multiple surface cracks that are arrayed in the loading direction has not received sufficient attention in the existing literature. For example, such cracks under tension will experience mixed-mode deformation [40]. Notwithstanding, the method developed in this study can be used to deal with such an issue. Two parallel surface cracks, identical in both shape and dimensions, were considered under remote tension, as depicted in Fig. 7. This problem was first analysed by Isida *et al.* [40] using two similar cracks with $b/a \leq 1.0$ and $c/b \geq 1$. In this study, analysis was performed for b/a ranging from 0.1 to 10 and c/b ranging from 0.1 to 5. Table 3(a) documents the values of the interaction factor, γ_{B}, defined as the ratio of the dimensionless SIF at point B (*i.e.*, crack-bottom) to that of a single crack under the same loading condition. These values are plotted in Fig. 8. The result indicates that an interaction of cracks led to the reduction in the Mode I SIF. The interaction effect depended on the aspect ratio of the cracks. A shallower crack tended to demonstrate a greater interaction effect; however, as the two cracks got very close, the aspect ratio dependence appeared to diminish. Furthermore, the existence of K_{II} and K_{III} was confirmed in this example. Table 3(b) lists the dimensionless Mode II SIF, $F_{\mathrm{II}}^{\mathrm{B}}$, at point B. In most cases, the K_{II} and K_{III} values were insignificant when compared with K_{I}. Consequently, they were not expected to affect the fracture strength (*e.g.*, fatigue strength) in practical problems but could play a major role in the determination of crack-growth direction. However, Modes II and III SIFs showed considerable increase for very shallow cracks, as noted in Table 3(b). For example, when $b/a = 0.1$ and $c/b = 0.5$, $F_{\mathrm{II}}^{\mathrm{B}} = 0.27$ and $F_{\mathrm{I}}^{\mathrm{B}} = 0.49$. In this case, $F_{\mathrm{II}}^{\mathrm{B}}$ was about 55 % of $F_{\mathrm{I}}^{\mathrm{B}}$ and might therefore no longer be

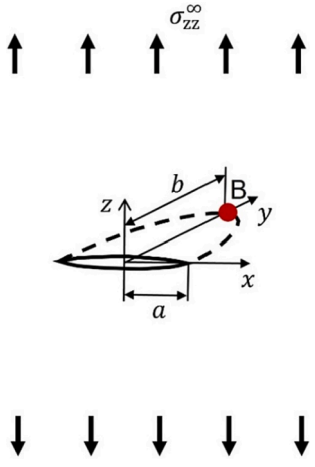

Fig. 5. Semi-elliptical surface crack under tension loading.

Table 2
Stress intensity factors for semi-elliptical surface cracks under tension loading.

b/a	$F_{IA} = K_{IA}/\sigma_{zz\infty}\sqrt{\pi a}$	$F_{IB} = K_{IB}/\sigma_{zz\infty}\sqrt{\pi b}$
0.1	0.355	1.096
0.5	0.517	0.864 (0.872*)
1	0.705 (0.713*)	0.656 (0.640*)
5	1.051	0.219
10	1.101	0.118

*Result obtained by Murakami. [Murakami, 1985]. In that study, Poisson's ratio was $\nu = 0.3$.

negligible in fracture strength assessment. Moreover, this type of Mode I crack interaction can play a positive role for fracture strength as compared to the case of a single crack [51,52].

A natural extension of the problem in Fig. 7 is the case where there are more than two similar, parallel and aligned surface cracks under remote tension. The results of such investigations will be useful in addressing practical fracture problems related to surface roughness due to manufacturing methods such as machining and additive manufacturing. Analyses were performed for N, an odd number of parallel and aligned surface cracks under tension (as shown in Fig. 9) for different combinations of c/b and b/a ratios, with emphasis on the interaction effects of the outermost and middle cracks. Table 4 details the dimensionless SIFs and interaction factors, γ_B, at point B. When available, the results from the study by Isida *et al.* [40] are provided in parentheses for comparison. It is noteworthy to highlight that in the Isida study, Poisson's ratio was set to 0.3 while it was fixed at zero in this study, perhaps the reason for the variation in results. Notwithstanding, for all practical purposes, the disparity appears to be minor. The obtained γ_B values are shown in Fig. 10. In all cases, the γ_B of the middle crack (dashed line) was always lower than that of the outermost crack (solid line). For a constant c/b ratio, the difference in γ_B values between the outermost and middle crack was dependent on the aspect ratio. In addition, the degree of interaction was minimally affected by the number of cracks, N. In fact, in all the cases analysed, the γ_B was almost constant for $N \geq 5$. The result suggests that analytical and experimental studies of this nature can be executed with five cracks and the outcomes would be equally applicable to a larger number of cracks. This will lead to considerable savings insofar as effort and resources are concerned.

4.3. Two parallel non-aligned cracks of identical shape but different sizes under tension

In the previous example, two parallel interacting cracks were of the same shape and size while the distance between the cracks varied. The cracks were also perfectly aligned perpendicular to the loading direction. However, in reality, many practical problems involve parallel interacting cracks that are not necessarily of the same size and most probably not aligned. In this example, two interacting, parallel surface cracks of similar shape but different sizes under tension were investigated, as well as the effect of non-alignment of the cracks (*cf.* Fig. 11). The distance between the two cracks in the loading direction was fixed to 125 % of the minor radius of Crack 2. The result for the dimensionless SIFs at points A, B and C, as well as the corresponding interaction factors for both cracks, are reported in Tables 5(a), 5(b) and 5(c) for $\alpha = 0$, $\alpha = 0.5$ and $\alpha = 1.0$, respectively. The obtained interaction factors, γ_{B_1} and γ_{B_2}, are correspondingly presented in Fig. 12(a) and 12(b). The effect of the difference in size of two interacting geometrically-similar cracks could clearly be seen. The interaction effect was more significant in the smaller crack (Crack 2) than in the larger crack (Crack 1). In all of the

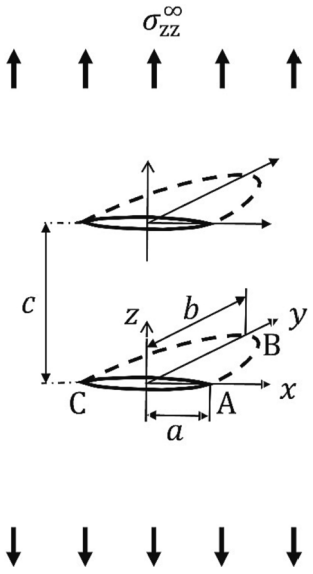

Fig. 7. Two parallel cracks under tension loading.

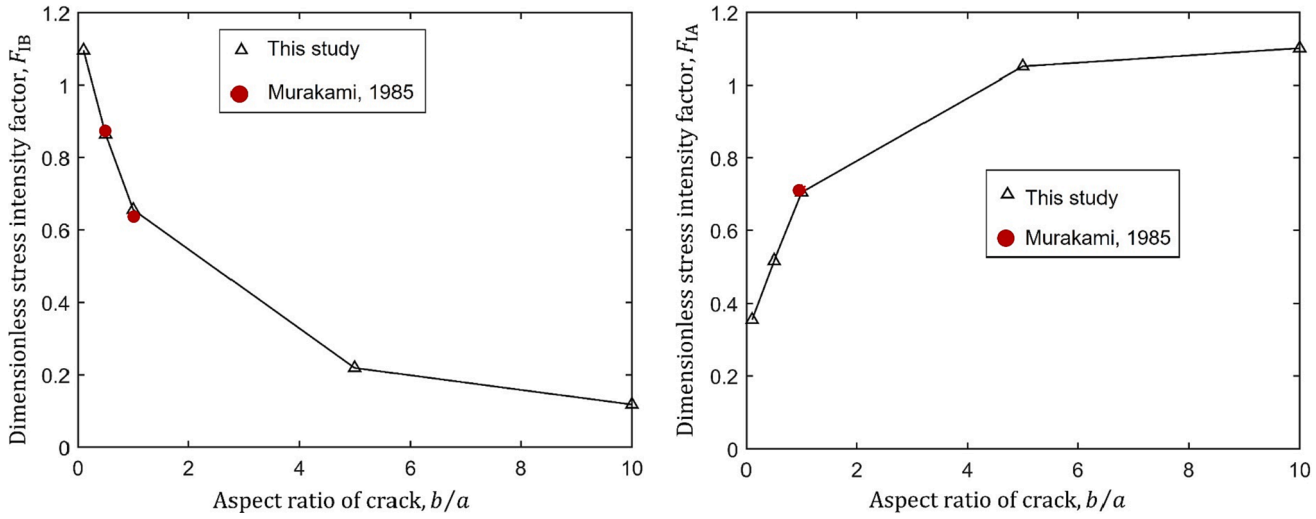

Fig. 6. (a). Dimensionless Mode I SIF at point B in Fig. 5. (b). Dimensionless Mode I SIF at point A in Fig. 5.

Table 3a
The γ_B for two similar and parallel, semi-elliptical surface cracks under tension loading.

$\frac{b}{a}$		0.1 (1.096)	0.25 (1.026)	0.5 (0.864)	1 (0.656)	2 (0.439)	5 (0.219)	10 (0.118)
$\frac{c}{b}$	5	0.93	0.94	0.97	0.98	0.99	0.99	1.00
	2	0.78	0.79	0.83	0.89	0.96	0.99	0.99
	1	0.65	0.66	0.69	0.76	0.86	0.96	0.98
	0.5	0.49	0.51	0.57	0.62	0.69	0.85	0.95
	0.25	0.48	0.50	0.52	0.52	0.56	0.67	0.82
	0.1	0.48	0.48	0.49	0.49	0.49	0.51	0.58

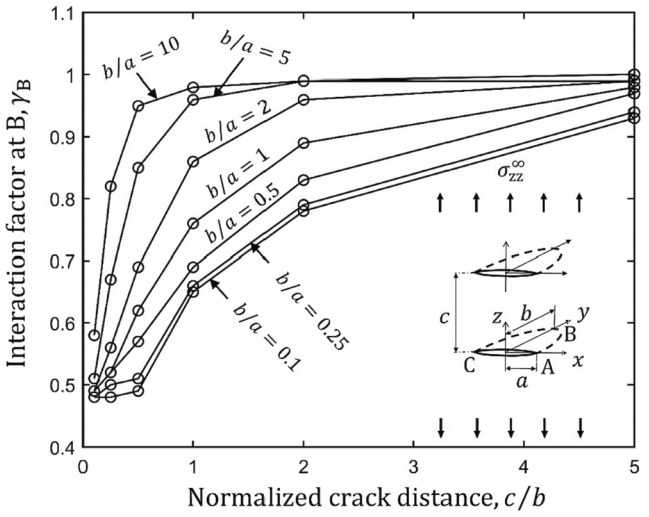

Fig. 8. Interaction factors at point B in Fig. 7.

Table 3b
The F_{II}^{B} for two similar and parallel, semi-elliptical surface cracks under tension loading.

$\frac{b}{a}$		0.1	0.25	0.5	1	2	5	10
$\frac{c}{b}$	5	0.018	0.014	0.007	0.002	0.001	0.000	0.000
	2	0.106	0.095	0.064	0.028	0.008	0.001	0.000
	1	0.190	0.170	0.126	0.072	0.029	0.003	0.001
	0.5	0.272	0.241	0.149	0.093	0.043	0.008	0.002
	0.25	0.161	0.112	0.073	0.088	0.036	0.009	0.003
	0.1	0.101	0.043	0.029	0.014	0.026	0.002	0.001

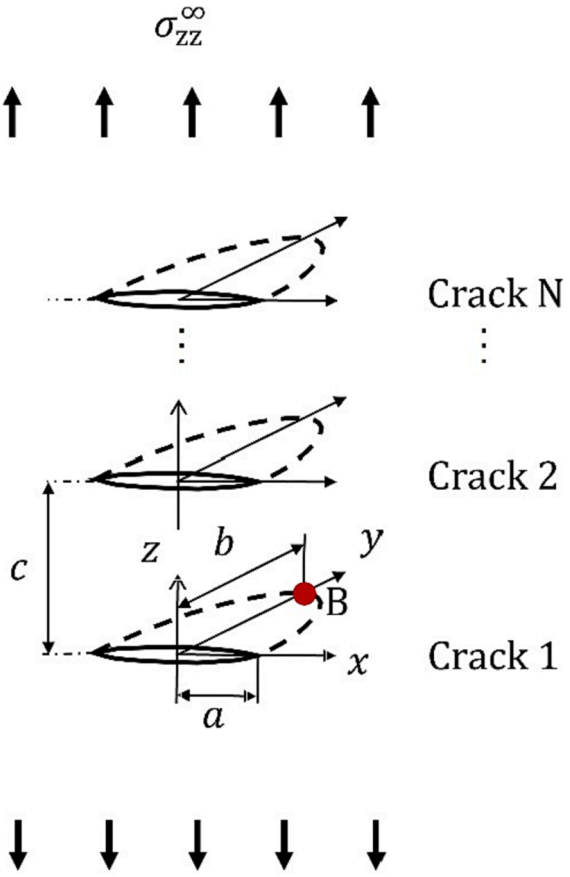

Fig. 9. *N* number of parallel cracks under tension loading.

cases, as α increased from 0 to 1, the nature of the interaction effect changed from reduction to amplification. The aspect ratio of the interacting cracks also influenced the interaction factors. In general, the nature of the interaction effect (reduction or amplification) is dependent on both the size difference and relative positions of the cracks. Based on these observations, the general perception that the interaction of two parallel and aligned cracks under tension always leads to a reduction in SIF is only valid for cracks that are geometrically similar and identical in size.

4.4. Random array of semi-elliptical surface cracks under tension

Previous examples have demonstrated the factors affecting the interaction of two cracks in proximity. However, in many practical cases, there are usually more than two cracks that form a colony, with all cracks interacting together. For example, multiple fatigue cracks initiate from surface defects during the fracture process of additively-manufactured components and cast parts. Corrosion fatigue applications are also similar examples of interaction between more than two surface cracks. In this sub-section, the combined interaction effect of surrounding cracks on a main crack is investigated. In Fig. 13, the main crack (Crack 1) surrounded by six neighbouring cracks was subjected to tensile loading. The aspect ratios of the cracks and their relative positions are indicated in Fig. 13. The aim of the investigation was to study the interaction effect of the surrounding cracks on K_I of Crack 1 at points A, B and C. Firstly, each surrounding crack was paired with Crack 1, then all seven cracks were examined together. The results are reported in Table 6. The results revealed that due to the interaction effect of the surrounding cracks, K_I at points A and C of Crack 1 was no longer the same, thus predicting different crack behaviour at both ends in terms of crack propagation or arrest. While the interaction effect gave rise to a 95 % reduction in K_I at point A, it provoked an increase of about 9 % in K_I at point C of Crack 1. This suggests the likely possibility of crack arrest at point A due to the presence of the surrounding cracks, whereas the growth rate of the crack-tip at point C would have been greater than that

Table 4
The F_I and γ_B for N similar and parallel, semi-elliptical surface cracks under tension loading.

		N	$F_{IB}^{outermost}$	F_{IB}^{middle}	$\gamma_B^{outermost}$	γ_B^{middle}
		3	0.4963	0.3431	0.757	0.523
		5	0.4893	0.3401	0.756	0.518
		9	0.4860	0.3322	0.741	0.506
	$\frac{b}{a}=1.0$	13	0.4850	0.3308	0.739	0.504
		17	0.4846	0.3304	0.739	0.504
		21	0.4844	0.3301	0.738	0.503
		25	0.4843	0.3300	0.738	0.503
$\frac{c}{b}=1.0$		29	0.4842	0.3300	0.738	0.503
		3	0.3717	0.3169	0.847	0.722
		5	0.3680	0.3066	0.838	0.698
		9	0.3663	0.3022	0.834	0.688
	$\frac{b}{a}=2.0$	13	0.3659	0.3015	0.834	0.687
		17	0.3657	0.3013	0.833	0.686
		21	0.3656	0.3012	0.833	0.686
		25	0.3656	0.3011	0.833	0.686
		29	0.3656	0.3011	0.833	0.686
		3	0.7071 (0.734*)	0.5709 (0.619*)	0.818	0.661
		5	0.6998 (0.726*)	0.5553 (0.593*)	0.810	0.643
	$\frac{b}{a}=0.5$	9	0.6968	0.5469	0.807	0.633
		13	0.6960	0.5457	0.806	0.632
		17	0.6957	0.5453	0.805	0.631
		21	0.6956	0.5451	0.805	0.631
$\frac{c}{b}=2.0$		25	0.6955	0.5450	0.805	0.631
		29	0.6954 (0.714*)	0.5450 (0.568*)	0.805	0.631
		3	0.5814	0.5203	0.886	0.793
		5	0.5780	0.5091	0.881	0.776
		9	0.5766	0.5049	0.879	0.770
	$\frac{b}{a}=1.0$	13	0.5762	0.5044	0.878	0.769
		17	0.5761	0.5042	0.878	0.769
		21	0.5761	0.5041	0.878	0.768
		25	0.5760	0.5041	0.878	0.768
		29	0.5760	0.5040	0.878	0.768

*Result obtained by Isida *et al.* [Isida, 1991]. In that study, Poisson's ratio was $\nu = 0.3$.

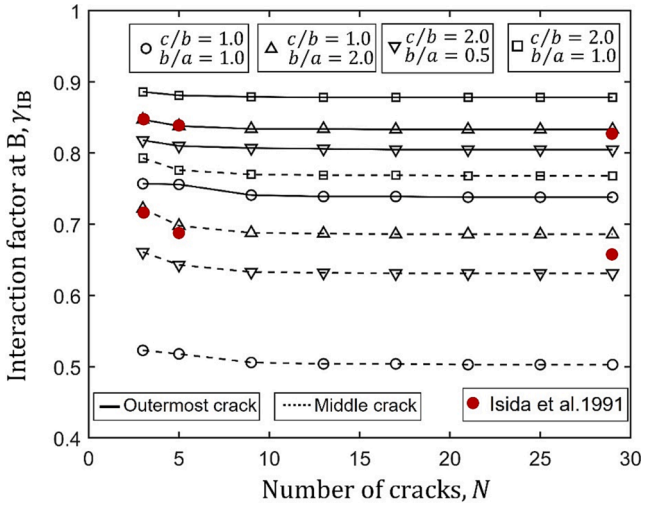

Fig. 10. Interaction factors at point B in Fig. 9.

of an isolated crack of the same size and loading condition. Furthermore, this example illustrates that all the surrounding cracks contributed to the interaction effects on the main cracks, the degree of which varied depending on their relative sizes, aspect ratios and distances. In this case, Crack 3 appears to have had the greatest influence on the

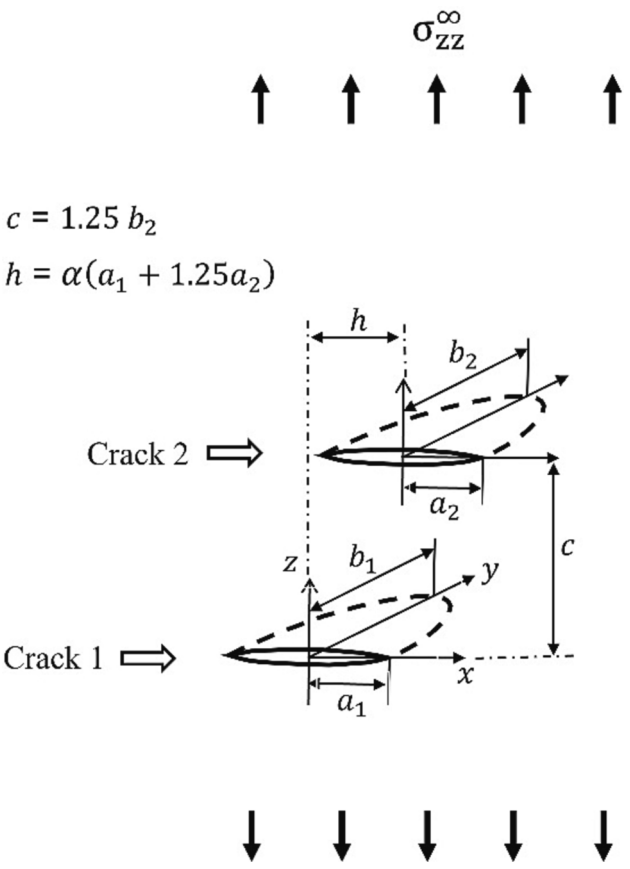

Fig. 11. Two staggered cracks under tension loading.

interaction effect, but this cannot easily be predicted prior to the analysis. It should be noted that the blueprint for designing this example was re-constructed from an actual crack colony observed in a corrosion fatigue test reported by Kitagawa *et al.* [8], *i.e.*, the locations and sizes of the cracks were measured directly according to their experimental results. The aspect ratio of every crack was assumed to be 1.0 in this study.

5. Material quality assessment method using fracture Mechanics-based Monte-Carlo simulation

It is an established fact that material cleanliness plays a crucial role in the structural strength of components. This is because material defects such as non-metallic inclusions, voids, cavities and corrosion pits often act as the primary roots of fracture. Conventional standards for the ranking of materials for quality control (*e.g.*, ISO 4967 [53], JIS G-0555 [54] and ASTM E45 [55]) typically fall into two categories. One is the qualitative approach which promotes the visual comparison of the sizes of defects found on a sample surface, while the other is rather quantitative, involving the measurement of the size and number of defects in an inspection area. However, the application limitations of these procedures have been pointed out by Murakami [56]. The primary problem is that these methods for evaluating material cleanliness do not take the fracture processes into account. Hence, the results obtained via the existing techniques cannot always be useful for ranking materials against the real fracture phenomena. Murakami [56] proposed to apply the statistics of extremes to the prediction of the maximum defect size (*e.g.*, non-metallic inclusion) contained in a given control volume in materials. The noteworthy merit of statistics of extremes is that it can allow for the effect of control volume, *i.e.*, the maximum defects included in manufacture naturally increase with a rise in sample population. This fact is completely ignored in the aforementioned conventional standards. However, the Murakami method does not consider the spatial

Table 5a
The F_I, γ_A, γ_B and γ_C for two staggered, semi-elliptical surface cracks under tension loading.$\alpha = 0$

b_2/b_1	b/a	F_{IA_1}	F_{IB_1}	F_{IC_1}	F_{IA_2}	F_{IB_2}	F_{IC_2}	γ_{A_1}	γ_{B_1}	γ_{C_1}	γ_{A_2}	γ_{B_2}	γ_{C_2}
0.5	0.25	0.468	1.043	0.468	0.001	0.091	0.001	1.01	1.02	1.01	0.002	0.09	0.002
	0.5	0.522	0.873	0.522	0.017	0.089	0.017	1.01	1.01	1.01	0.03	0.10	0.03
	1.0	0.705	0.659	0.706	0.064	0.078	0.063	1.00	1.01	1.00	0.09	0.12	0.09
	1.5	0.818	0.527	0.818	0.138	0.087	0.138	0.99	1.00	0.99	0.17	0.17	0.17
	2.0	0.885	0.439	0.885	0.233	0.106	0.233	0.99	1.00	0.99	0.26	0.24	0.26
0.75	0.25	0.422	0.924	0.422	0.043	0.267	0.043	0.91	0.90	0.91	0.09	0.26	0.09
	0.5	0.459	0.770	0.459	0.099	0.271	0.099	0.89	0.89	0.89	0.19	0.31	0.19
	1.0	0.622	0.589	0.622	0.249	0.258	0.249	0.88	0.89	0.88	0.35	0.39	0.35
	1.5	0.729	0.476	0.729	0.395	0.255	0.395	0.89	0.90	0.89	0.48	0.48	0.48
	2.0	0.797	0.400	0.797	0.515	0.251	0.515	0.89	0.91	0.89	0.57	0.57	0.57
1.0	0.25	0.237	0.618	0.237	0.237	0.618	0.237	0.51	0.60	0.51	0.51	0.60	0.51
	0.5	0.297	0.555	0.297	0.297	0.555	0.297	0.57	0.64	0.57	0.57	0.64	0.57
	1.0	0.474	0.459	0.474	0.474	0.459	0.474	0.67	0.70	0.67	0.67	0.70	0.67
	1.5	0.606	0.396	0.606	0.606	0.396	0.606	0.74	0.75	0.74	0.74	0.75	0.74
	2.0	0.697	0.349	0.699	0.697	0.349	0.699	0.78	0.79	0.78	0.78	0.79	0.78

Table 5b
The F_I, γ_A, γ_B and γ_C for two staggered, semi-elliptical surface cracks under tension loading.$\alpha = 0.5$

b_2/b_1	b/a	F_{IA_1}	F_{IB_1}	F_{IC_1}	F_{IA_2}	F_{IB_2}	F_{IC_2}	γ_{A_1}	γ_{B_1}	γ_{C_1}	γ_{A_2}	γ_{B_2}	γ_{C_2}
0.5	0.25	0.531	1.056	0.465	0.544	0.726	0.027	1.15	1.03	1.01	1.18	0.71	0.06
	0.5	0.550	0.882	0.522	0.630	0.548	0.072	1.06	1.02	1.01	1.22	0.63	0.14
	1.0	0.624	0.667	0.713	0.806	0.514	0.289	0.89	1.02	1.01	1.14	0.78	0.41
	1.5	0.704	0.535	0.836	0.874	0.425	0.427	0.85	1.02	1.02	1.06	0.81	0.52
	2.0	0.779	0.445	0.912	0.888	0.349	0.508	0.87	1.01	1.02	0.99	0.79	0.57
0.75	0.25	0.397	1.015	0.462	0.469	0.975	0.116	0.86	0.99	1.00	1.02	0.95	0.25
	0.5	0.430	0.877	0.523	0.546	0.855	0.230	0.83	1.02	1.01	1.06	0.99	0.45
	1.0	0.551	0.676	0.725	0.765	0.654	0.423	0.78	1.03	1.03	1.09	0.99	0.60
	1.5	0.658	0.536	0.849	0.866	0.502	0.550	0.80	1.02	1.03	1.05	0.95	0.67
	2.0	0.743	0.440	0.917	0.900	0.403	0.631	0.83	1.00	1.02	1.00	0.92	0.70
1.0	0.25	0.275	0.990	0.462	0.462	0.990	0.275	0.59	0.96	1.00	1.00	0.96	0.59
	0.5	0.346	0.875	0.528	0.528	0.875	0.346	0.70	1.01	1.02	1.02	1.01	0.70
	1.0	0.509	0.668	0.736	0.735	0.668	0.510	0.72	1.02	1.04	1.04	1.02	0.72
	1.5	0.627	0.520	0.847	0.846	0.520	0.627	0.76	0.99	1.03	1.03	0.99	0.76
	2.0	0.713	0.422	0.898	0.897	0.422	0.714	0.79	0.96	1.00	0.99	0.96	0.79

Table 5c
The F_I, γ_A, γ_B and γ_C for two staggered, semi-elliptical surface cracks under tension loading.$\alpha = 1.0$

b_2/b_1	b/a	F_{IA_1}	F_{IB_1}	F_{IC_1}	F_{IA_2}	F_{IB_2}	F_{IC_2}	γ_{A_1}	γ_{B_1}	γ_{C_1}	γ_{A_2}	γ_{B_2}	γ_{C_2}
0.5	0.25	0.465	1.028	0.463	0.469	1.053	0.485	1.01	1.00	1.00	1.02	1.03	1.05
	0.5	0.528	0.869	0.519	0.540	0.921	0.586	1.02	1.01	1.00	1.04	1.07	1.13
	1.0	0.737	0.664	0.712	0.773	0.738	0.859	1.05	1.01	1.01	1.09	1.13	1.22
	1.5	0.863	0.535	0.836	0.926	0.605	0.992	1.05	1.02	1.02	1.12	1.15	1.20
	2.0	0.929	0.446	0.911	1.014	0.503	1.038	1.04	1.02	1.02	1.13	1.15	1.16
0.75	0.25	0.468	1.031	0.463	0.466	1.039	0.475	1.01	1.01	1.00	1.01	1.01	1.03
	0.5	0.535	0.875	0.522	0.529	0.893	0.556	1.04	1.01	1.01	1.02	1.03	1.08
	1.0	0.748	0.672	0.719	0.739	0.698	0.788	1.06	1.03	1.02	1.05	1.06	1.12
	1.5	0.866	0.542	0.845	0.874	0.565	0.903	1.05	1.03	1.03	1.06	1.07	1.10
	2.0	0.922	0.452	0.920	0.951	0.469	0.950	1.03	1.03	1.03	1.06	1.07	1.06
1.0	0.25	0.469	1.034	0.464	0.464	1.034	0.469	1.02	1.01	1.00	1.00	1.01	1.02
	0.5	0.541	0.881	0.524	0.524	0.881	0.541	1.05	1.02	1.01	1.01	1.02	1.05
	1.0	0.753	0.680	0.725	0.725	0.680	0.754	1.07	1.04	1.03	1.03	1.04	1.07
	1.5	0.863	0.548	0.852	0.852	0.548	0.863	1.05	1.04	1.03	1.03	1.04	1.05
	2.0	0.914	0.454	0.926	0.925	0.455	0.915	1.02	1.03	1.03	1.03	1.04	1.02

distribution of defects and therefore cannot evaluate the possible interaction effects of cracks that might initiate from the defects. This type of scenario has been reported in corrosion fatigue problems where fatigue cracks initiate from distributed corrosion pits formed by chemical reactions between inclusions and a corrosive environment [8,57,58]. It was also reported that, in additively-manufactured and cast components, crack interactions cannot be ignored for the colony of surface cracks initiated from defects [56,2]. In such cases, the quality

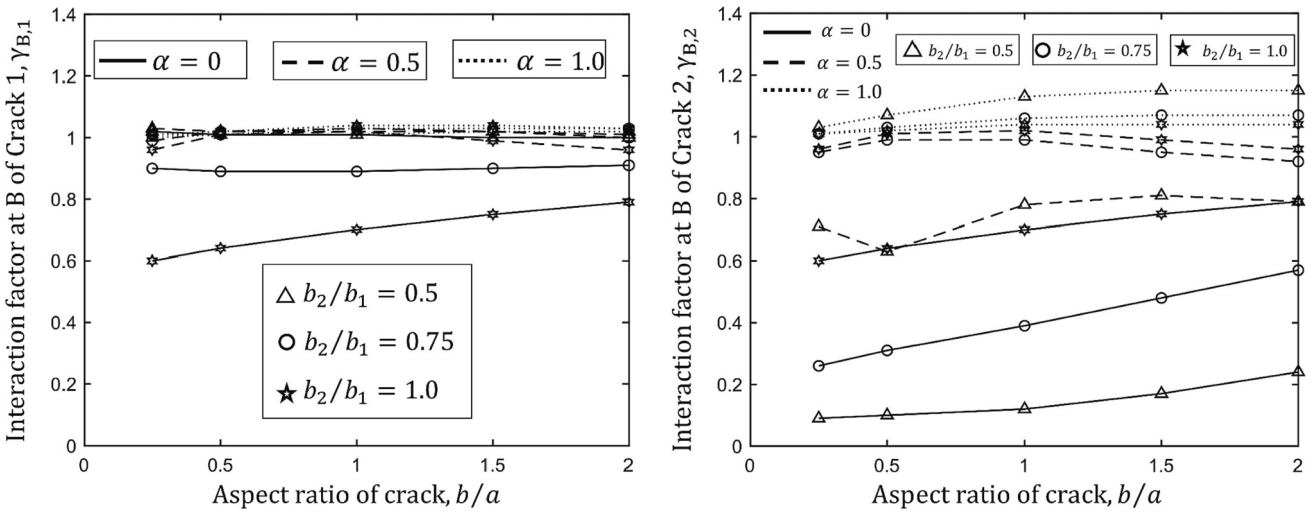

Fig. 12. (a). Interaction factor at point B of Crack 1 in Fig. 11. (b). Interaction factor at point B of Crack 2 in Fig. 11.

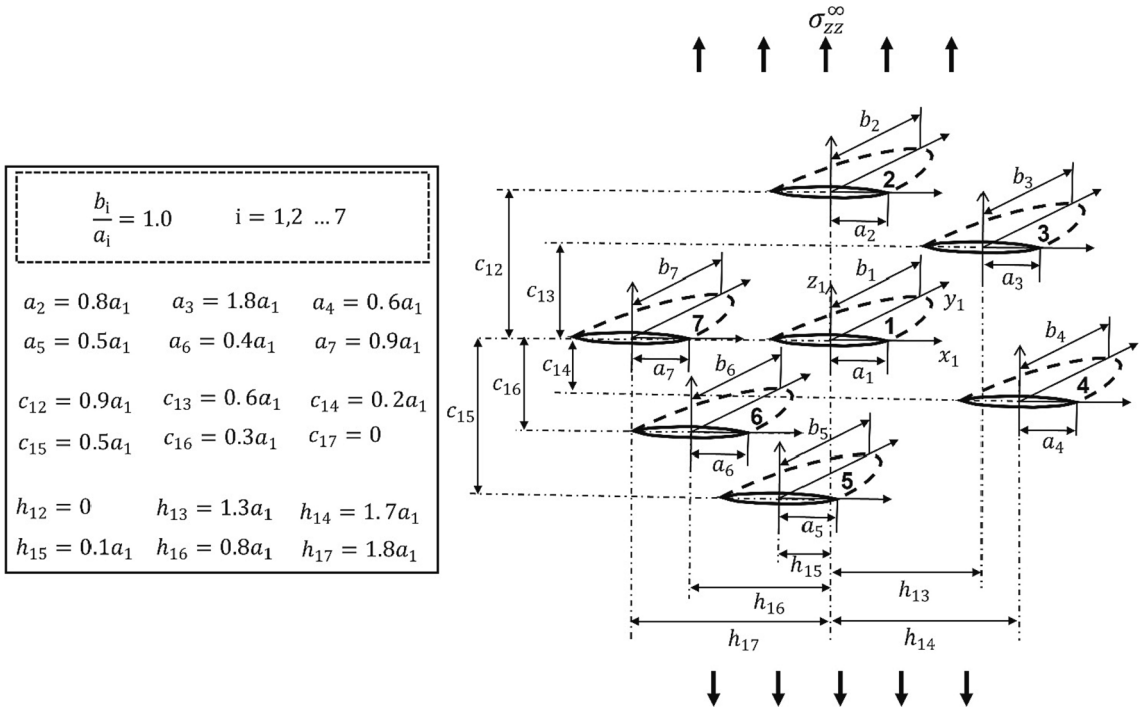

Fig. 13. Influence of six surrounding cracks on a main crack under tension loading.

Table 6
Interaction factors, γ_A, γ_B and γ_C for Crack 1 with surrounding cracks.

	γ_{1A}^{1}	γ_{1B}^{1}	γ_{1C}^{1}
Crack 1 and 2 only	0.86	0.87	0.86
Crack 1 and 3 only	0.36	0.65	1.14
Crack 1 and 4 only	1.08	1.02	1.02
Crack 1 and 5 only	1.00	0.99	0.98
Crack 1 and 6 only	1.01	1.01	0.97
Crack 1 and 7 only	1.05	1.06	1.25
All cracks	0.05	0.54	1.09

control of materials should bear in mind the spatial distribution of defects and cracks. As a solution, the numerical analysis developed in the present study can be a novel ranking methodology, used in conjunction with the Monte Carlo simulation technique. The following case study will provide context for demonstrating the procedure.

On a monthly basis, a particular company received thousands of batches of certain load-carrying cast components from supplier A. However, due to changes in the company's policy, the management decided to switch from supplier A to supplier B. Inclusion analysis for batches from the respective suppliers showed that inclusions over an inspected area in batch A were larger in size than those in batch B, although they were less dense in A than in B. The aim of this study was to determine which batch was cleaner from the viewpoint of the fracture process, when a component was primarily subjected to tensile loading, as shown in Fig. 14. Such a judgement should include the statistical nature of both the sizes and locations of the defects in the materials. The results from quantitative inclusion measurements using polished samples from batches A and B are recorded in Table 7.

Assuming that the non-metallic inclusions were randomly distributed in both batches, any cracks initiating from those inclusions would

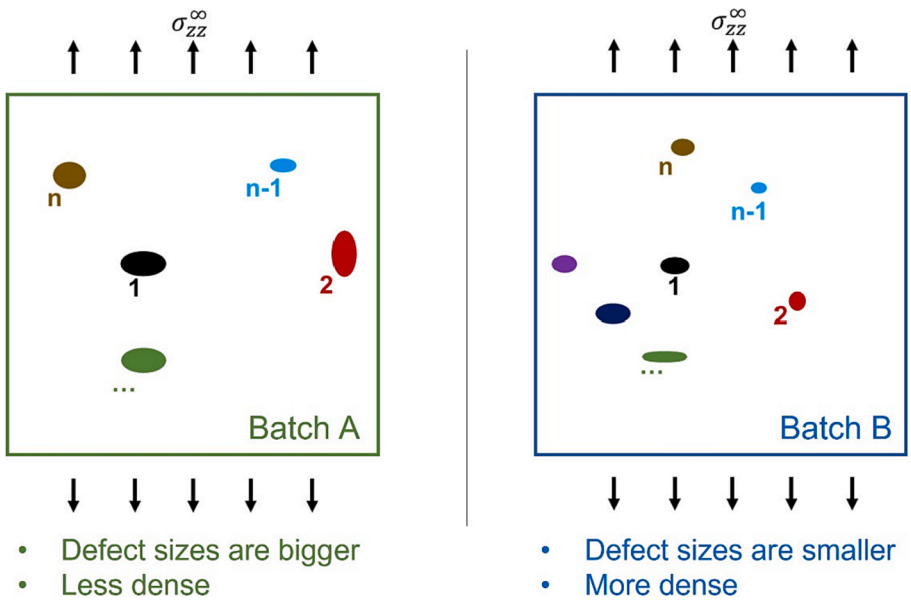

Fig. 14. Inclusions from two different batches.

be expected to follow a similar spatial distribution, *i.e.*, the spatial distribution of inclusions can serve as a blueprint for that of initiated cracks. In this analysis, semi-elliptical surface cracks with aspect ratios of 0.5 were presumed for both batches. The Monte-Carlo simulation procedure was then incorporated. For each batch, 100 "virtual" specimens were generated by the Monte-Carlo engine for two containers, namely containers A and B, fabricated from batches A and B, respectively. In other words, 200 "virtual" specimens were generated in total. Next, 25 cracks were distributed on the surfaces of each specimen, with the statistical distribution of the crack sizes and locations reflecting the statistical data reported in Table 7. The simulation included 100 iterations, with each iteration using a pair of "virtual" specimens, one extracted from container A and the other from container B. Under tension, the maximum SIFs in the specimens from containers A and B, $K_{\mathrm{I,A}}^{\max}$ and $K_{\mathrm{I,B}}^{\max}$, were reported for each run. After n iterations, n_{A} is the number of times for $K_{\mathrm{I,A}}^{\max} < K_{\mathrm{I,B}}^{\max}$, similarly n_{B} is that for $K_{\mathrm{I,B}}^{\max} < K_{\mathrm{I,A}}^{\max}$. The output results after each iteration were:

$\mathrm{Prob_B} = \frac{n_{\mathrm{B}}}{n}$, Probability that batch B was cleaner than batch A.

$\mathrm{Prob_A} = \frac{n_{\mathrm{A}}}{n}$, Probability that batch A was cleaner than batch B.

The result from the 100 iterations is reported in Fig. 15. The entire simulation took about 13 h to complete. It was intriguing to follow how the probabilities evolved with the number of iterations. During the first 10 iterations, the contest was nearly a draw, but a difference began to emerge after about 20 iterations and stabilized after about 40. Statistically, the conclusion to be drawn from the simulation is that there was a 0.77 probability that a random sample from batch B was cleaner than one from batch A; hence, batch B was judged to be "cleaner" under the present circumstances. The result predicted that if 100 real tensile tests were to be performed using pairs of specimens from the two batches, the breaking load for batch B would exceed that of batch A in 77 cases. It is also noted that another advantage of the method proposed here is that it can consider the effect of the actual loading type in the determination of a cleanliness ranking. Indeed, it would be interesting if a similar simulation were to be conducted for shear loading and multiaxial loading.

Table 7
Quantitative inclusion measurements of samples from Batches C and K.

	Density	Mean length,μm	Standard deviation of length
Batch C (Supplier C)	89.0	6.78	1.47
Batch K (Supplier K)	69.5	9.19	1.61

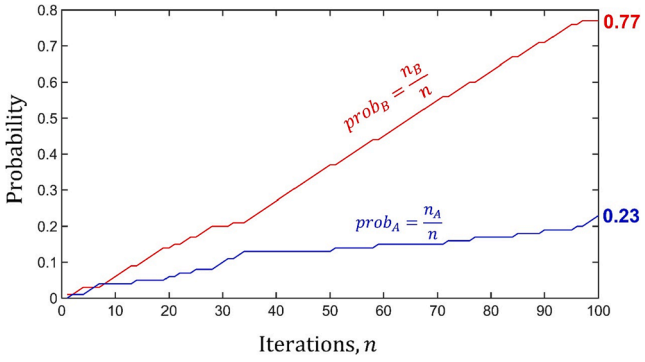

Fig. 15. Monte-Carlo simulation of virtual samples from Batches A and B.

Such a study could lead to remarkable findings about the effects of loading types on material quality assessment.

6. Conclusions

1) A novel procedure for the determination of SIFs of multiple 3-D cracks was established. The method is based on the distributed dislocation method, an eigenstrain technique.
2) Numerical calculations were performed for multiple non-planar, semi-elliptical surface cracks under tension. Some examples were implemented to elucidate the effects of aspect ratio, spacing distance in the loading direction, difference in size and non-alignment of parallel cracks on the nature of the interaction effect.
3) The pioneering study revealed the effect of randomly-distributed surrounding cracks on the Mode I stress intensity factor of a main crack.
4) The innovative multiple 3-D crack analysis procedure was combined with the Monte-Carlo simulation approach to develop a new method for material quality assessment, in consideration of the interaction effect of distributed material defects and loading types.

Funding

This research did not receive any specific grant from funding agencies in the public, commercial, or not-for-profit sectors.

Data Availability

The raw data required to reproduce these findings cannot be shared at this time as the data also forms part of an ongoing study.

CRediT authorship contribution statement

Adeyinka Abass: Conceptualization, Software, Investigation, Writing – original draft. **Hisao Matsunaga:** Supervision, Funding acquisition, Writing – review & editing.

Declaration of Competing Interest

The authors declare that they have no known competing financial interests or personal relationships that could have appeared to influence the work reported in this paper.

Data availability

Data will be made available on request.

Appendix A

Derivatives of Stress Components from Points Load - Green Function.

$$\begin{aligned}\frac{d\sigma_{zz}^{P}}{d\zeta}=\frac{1}{8\pi(1-\nu)}\Bigg[&-\frac{3(1-2\nu)(z-\zeta)^2}{R_1^5}+\frac{1-2\nu}{R_1^3}+\frac{3(1-2\nu)(5-4\nu)(z-\zeta)^2}{R_2^5}-\frac{(1-2\nu)(5-4\nu)}{R_2^3}+\frac{9(z-\zeta)^2}{R_1^5}-\frac{15(z-\zeta)^4}{R_1^7}-\frac{15(3-4\nu)(z-\zeta)^4}{R_2^7}\\&+\frac{9(3-4\nu)(z-\zeta)^2}{R_2^5}+\frac{12(1-2\nu)(1-\nu)}{R_2(R_2+y+\eta)^2}-\frac{24(1-2\nu)(1-\nu)(z-\zeta)^2}{{R_2}^2(R_2+y+\eta)^3}-\frac{12(1-2\nu)(1-\nu)(z-\zeta)^2}{{R_2}^3(R_2+y+\eta)^2}+\frac{12(1-2\nu)(1-\nu)(3R_2+y+\eta)(z-\zeta)^4}{{R_2}^4(R_2+y+\eta)^4}\\&-\frac{12(1-2\nu)(1-\nu)(z-\zeta)^4}{{R_2}^4(R_2+y+\eta)^3}-\frac{12(1-2\nu)(1-\nu)(3R_2+y+\eta)(z-\zeta)^2}{{R_2}^3(R_2+y+\eta)^3}+\frac{12(1-2\nu)(1-\nu)(3R_2+y+\eta)(z-\zeta)^4}{{R_2}^5(R_2+y+\eta)^3}+\frac{90\eta^2(z-\zeta)^2}{R_2^7}-\frac{18\eta^2}{R_2^5}\\&-\frac{30(3-2\nu)(y+\eta)(z-\zeta)^2}{R_2^7}+\frac{6(3-2\nu)\eta(y+\eta)}{R_2^5}+\frac{210y\eta(z-\zeta)^4}{R_2^9}-\frac{90y\eta(z-\zeta)^2}{R_2^7}\Bigg]\end{aligned}\tag{A.1}$$

$$\begin{aligned}\frac{d\sigma_{zz}^{Q}}{d\xi}=\frac{1}{8\pi(1-\nu)}\Bigg[&-\frac{1-2\nu}{R_1^3}+\frac{3(1-2\nu)(x-\xi)^2}{R_1^5}+\frac{3(1-2\nu)(3-4\nu)(x-\xi)^2}{R_2^5}-\frac{(1-2\nu)(3-4\nu)}{R_2^3}+\frac{3(z-\zeta)^2}{R_1^5}-\frac{15(x-\xi)^2(z-\zeta)^2}{R_1^7}\\&-\frac{15(3-4\nu)(x-\xi)^2(z-\zeta)^2}{R_2^7}+\frac{3(3-4\nu)(z-\zeta)^2}{R_2^5}+\frac{4(1-2\nu)(1-\nu)}{R_2(R_2+y+\eta)^2}-\frac{8(1-2\nu)(1-\nu)(x-\xi)^2}{{R_2}^2(R_2+y+\eta)^3}-\frac{4(1-2\nu)(1-\nu)(x-\xi)^2}{{R_2}^3(R_2+y+\eta)^2}\\&+\frac{12(1-2\nu)(1-\nu)(3R_2+y+\eta)(x-\xi)^2(z-\zeta)^2}{{R_2}^4(R_2+y+\eta)^4}-\frac{12(1-2\nu)(1-\nu)(x-\xi)^2(z-\zeta)^2}{{R_2}^4(R_2+y+\eta)^3}-\frac{4(1-2\nu)(1-\nu)(3R_2+y+\eta)(z-\zeta)^2}{{R_2}^3(R_2+y+\eta)^3}\\&+\frac{12(1-2\nu)(1-\nu)(3R_2+y+\eta)(x-\xi)^2(z-\zeta)^2}{{R_2}^5(R_2+y+\eta)^3}+\frac{30\eta^2(x-\xi)^2}{R_2^7}-\frac{6\eta^2}{R_2^5}-\frac{30(1-2\nu)(y+\eta)(x-\xi)^2}{R_2^7}+\frac{6(1-2\nu)\eta(y+\eta)}{R_2^5}\\&+\frac{210y\eta(x-\xi)^2(z-\zeta)^2}{R_2^9}-\frac{30y\eta(z-\zeta)^2}{R_2^7}\Bigg]\end{aligned}\tag{A.2}$$

$$\begin{aligned}\frac{d\sigma_{zz}^{R}}{d\eta}=\frac{1}{8\pi(1-\nu)}\Bigg[&-\frac{1-2\nu}{R_1^3}+\frac{3(1-2\nu)(y-\eta)^2}{R_1^5}+\frac{3(z-\zeta)^2}{R_1^5}-\frac{15(y-\eta)^2(z-\zeta)^2}{R_1^7}-\frac{3(1-2\nu)(y+\eta)(4\nu y+4\nu\eta+3\eta-3y)}{R_2^5}-\frac{(1-2\nu)(3-4\nu)}{R_2^3}\\&+\frac{6\eta(2\nu y-y+2\nu\eta)+3(3-4\nu)(z-\zeta)^2-6(1-2\nu)\eta(y+\eta)}{R_2^5}-\frac{15(y+\eta)\big((y-\eta)(z-\zeta)^2(3-4\nu)+2\eta(y+\eta)(2\nu y-y+2\eta\nu)\big)}{R_2^7}+\frac{30\eta(y+\eta)(z-\zeta)^2}{R_2^7}\\&+\frac{30y\eta(z-\zeta)^2}{R_2^7}-\frac{210y\eta(y-\eta)^2(z-\zeta)^2}{R_2^9}-\frac{4(1-2\nu)(1-\nu)(y+\eta)}{R_2^3(R_2+y+\eta)}-\frac{4\left(\frac{y+\eta}{R_2}+1\right)(1-2\nu)(1-\nu)}{R_2(R_2+y+\eta)^2}+\frac{8(1-2\nu)(1-\nu)(y+\eta)(z-\zeta)^2}{R_2^4(R_2+y+\eta)^2}\\&+\frac{8(1-2\nu)(1-\nu)(z-\zeta)^2\left(\frac{y+\eta}{R_2}+1\right)}{R_2^2(R_2+y+\eta)^3}+\frac{12(1-2\nu)(1-\nu)(y+\eta)(z-\zeta)^2}{R_2^5(R_2+y+\eta)}+\frac{4(1-2\nu)(1-\nu)(z-\zeta)^2\left(\frac{y+\eta}{R_2}+1\right)}{R_2^3(R_2+y+\eta)^2}\Bigg]\end{aligned}\tag{A.3}$$

$$\begin{aligned}\frac{d\sigma_{zz}^{P}}{d\xi}=\frac{1}{8\pi(1-\nu)}\Bigg[&-\frac{3(1-2\nu)(z-\zeta)(x-\xi)}{R_1^5}+\frac{3(1-2\nu)(5-4\nu)(z-\zeta)(x-\xi)}{R_2^5}-\frac{15(z-\zeta)^3(x-\xi)}{R_1^7}-\frac{15(3-4\nu)(z-\zeta)^3(x-\xi)}{R_2^7}\\&-\frac{24(1-2\nu)(1-\nu)(z-\zeta)(x-\xi)}{{R_2}^2(R_2+y+\eta)^3}-\frac{12(1-2\nu)(1-\nu)(z-\zeta)(x-\xi)}{{R_2}^3(R_2+y+\eta)^2}+\frac{12(1-2\nu)(1-\nu)(3R_2+y+\eta)(z-\zeta)^3(x-\xi)}{{R_2}^4(R_2+y+\eta)^4}-\frac{12(1-2\nu)(1-\nu)(z-\zeta)^3(x-\xi)}{{R_2}^4(R_2+y+\eta)^3}\\&+\frac{12(1-2\nu)(1-\nu)(3R_2+y+\eta)(z-\zeta)^3(x-\xi)}{{R_2}^5(R_2+y+\eta)^3}+\frac{90\eta^2(z-\zeta)(x-\xi)}{R_2^7}-\frac{30(3-2\nu)(y+\eta)(z-\zeta)(x-\xi)}{R_2^7}+\frac{210y\eta(z-\zeta)^3(x-\xi)}{R_2^9}\Bigg]\end{aligned}\tag{A.4}$$

$$\frac{d\sigma_{zz}^{Q}}{d\zeta}=\frac{1}{8\pi(1-\nu)}\left[\frac{3(1-2\nu)(z-\zeta)(x-\xi)}{R_1^5}+\frac{3(1-2\nu)(3-4\nu)(z-\zeta)(x-\xi)}{R_2^5}+\frac{6(z-\zeta)(x-\xi)}{R_1^5}-\frac{15(z-\zeta)^3(x-\xi)}{R_1^7}-\frac{15(3-4\nu)(z-\zeta)^3(x-\xi)}{R_2^7}\right.$$
$$+\frac{6(3-4\nu)(z-\zeta)(x-\xi)}{R_2^5}-\frac{8(1-2\nu)(1-\nu)(z-\zeta)(x-\xi)}{{R_2}^2(R_2+y+\eta)^3}-\frac{4(1-2\nu)(1-\nu)(z-\zeta)(x-\xi)}{{R_2}^3(R_2+y+\eta)^2}+\frac{12(1-2\nu)(1-\nu)(3R_2+y+\eta)(z-\zeta)^3(x-\xi)}{{R_2}^4(R_2+y+\eta)^4}$$
$$-\frac{12(1-2\nu)(1-\nu)(z-\zeta)^3(x-\xi)}{{R_2}^4(R_2+y+\eta)^3}-\frac{8(1-2\nu)(1-\nu)(3R_2+y+\eta)(z-\zeta)(x-\xi)}{{R_2}^3(R_2+y+\eta)^3}+\frac{12(1-2\nu)(1-\nu)(3R_2+y+\eta)(z-\zeta)^3(x-\xi)}{{R_2}^5(R_2+y+\eta)^3}$$
$$\left.+\frac{30\eta^2(z-\zeta)(x-\xi)}{R_2^7}-\frac{30(1-2\nu)\eta(y+\eta)(z-\zeta)(x-\xi)}{R_2^7}+\frac{210y\eta(z-\zeta)^3(x-\xi)}{R_2^9}-\frac{60\eta y(z-\zeta)(x-\xi)}{R_2^7}\right] \tag{A.5}$$

$$\frac{d\sigma_{zz}^{P}}{d\eta}=\frac{1}{8\pi(1-\nu)}\left[-\frac{3(1-2\nu)(z-\zeta)(y-\eta)}{R_1^5}+\frac{3(1-2\nu)(5-4\nu)(z-\zeta)(y+\eta)}{R_2^5}-\frac{15(z-\zeta)^3(y-\eta)}{R_1^7}-\frac{15(3-4\nu)(z-\zeta)^3(y+\eta)}{R_2^7}\right.$$
$$-\frac{12(1-2\nu)(1-\nu)(z-\zeta)(y+\eta)}{{R_2}^3(R_2+y+\eta)^2}-\frac{24(1-2\nu)(1-\nu)(z-\zeta)\left(\frac{y+\eta}{R_2}+1\right)}{R_2(R_2+y+\eta)^2}-\frac{4(1-2\nu)(1-\nu)(z-\zeta)^3\left(\frac{3(y+\eta)}{R_2}+1\right)}{{R_2}^3(R_2+y+\eta)^3}$$
$$+\frac{12(1-2\nu)(1-\nu)(z-\zeta)^3(y+\eta)(3R_2+y+\eta)}{{R_2}^5(R_2+y+\eta)^3}+\frac{12(1-2\nu)(1-\nu)(z-\zeta)^3(3R_2+y+\eta)\left(\frac{y+\eta}{R_2}+1\right)}{{R_2}^3(R_2+y+\eta)^4}+\frac{90\eta(z-\zeta)(y-\eta)^2}{R_2^7}+\frac{6\eta(3-2\nu)(z-\zeta)}{R_2^5}$$
$$\left.-\frac{30(3-2\nu)(z-\zeta)(y+\eta)^2}{R_2^7}-\frac{30\eta(z-\zeta)^3}{R_2^7}+\frac{210y\eta(z-\zeta)^3(y+\eta)}{R_2^9}\right] \tag{A.6}$$

$$\frac{d\sigma_{zz}^{R}}{d\zeta}=\frac{1}{8\pi(1-\nu)}\left[\frac{3(1-2\nu)(z-\zeta)(y-\eta)}{R_1^5}+\frac{6(z-\zeta)(y-\eta)}{R_1^5}-\frac{15(z-\zeta)^3(y-\eta)}{R_1^7}-\frac{3(1-2\nu)(z-\zeta)(4\nu y+4\nu\eta+3\eta-3y)}{R_2^5}\right.$$
$$-\frac{15(z-\zeta)\left[(3-4\nu)(y-\eta)(z-\zeta)^2+2\eta(2\nu\eta-y+2\nu\eta)(y+\eta)\right]}{R_2^7}+\frac{6(3-4\nu)(z-\zeta)(y-\eta)}{R_2^5}-\frac{210y\eta(z-\zeta)^3(y+\eta)}{R_2^9}+\frac{60\eta y(z-\zeta)(y+\eta)}{R_2^7}$$
$$\left.-\frac{12(1-2\nu)(1-\nu)(z-\zeta)}{{R_2}^2(R_2+y+\eta)^2}+\frac{12(1-2\nu)(1-\nu)(z-\zeta)^3}{{R_2}^4(R_2+y+\eta)^2}+\frac{8(1-2\nu)(1-\nu)(z-\zeta)^3}{{R_2}^3(R_2+y+\eta)^3}-\frac{12(1-2\nu)(1-\nu)(z-\zeta)}{{R_2}^3(R_2+y+\eta)}+\frac{12(1-2\nu)(1-\nu)(z-\zeta)^3}{{R_2}^5(R_2+y+\eta)}\right] \tag{A.7}$$

$$\frac{d\tau_{xz}^{P}}{d\zeta}=\frac{1}{8\pi(1-\nu)}\left[-\frac{3(1-2\nu)(z-\zeta)(x-\xi)}{R_1^5}+\frac{3(1-2\nu)(z-\zeta)(x-\xi)}{R_2^5}+\frac{6(z-\zeta)(x-\xi)}{R_1^5}-\frac{15(z-\zeta)^3(x-\xi)}{R_1^7}-\frac{15(3-4\nu)(z-\zeta)^3(x-\xi)}{R_2^7}\right.$$
$$+\frac{6(3-4\nu)(z-\zeta)(x-\xi)}{R_2^5}-\frac{8(1-2\nu)(1-\nu)(z-\zeta)(x-\xi)}{{R_2}^2(R_2+y+\eta)^3}-\frac{4(1-2\nu)(1-\nu)(z-\zeta)(x-\xi)}{{R_2}^3(R_2+y+\eta)^2}+\frac{12(1-2\nu)(1-\nu)(3R_2+y+\eta)(z-\zeta)^3(x-\xi)}{{R_2}^4(R_2+y+\eta)^4}$$
$$-\frac{12(1-2\nu)(1-\nu)(z-\zeta)^3(x-\xi)}{{R_2}^4(R_2+y+\eta)^3}-\frac{8(1-2\nu)(1-\nu)(3R_2+y+\eta)(z-\zeta)(x-\xi)}{{R_2}^3(R_2+y+\eta)^3}+\frac{12(1-2\nu)(1-\nu)(3R_2+y+\eta)(z-\zeta)^3(x-\xi)}{{R_2}^5(R_2+y+\eta)^3}$$
$$\left.-\frac{30y\eta(z-\zeta)(x-\xi)}{R_2^7}+\frac{210y\eta(z-\zeta)^3(x-\xi)}{R_2^9}-\frac{60\eta y(z-\zeta)(x-\xi)}{R_2^7}\right] \tag{A.8}$$

$$\frac{d\tau_{xz}^{Q}}{d\xi}=\frac{1}{8\pi(1-\nu)}\left[-\frac{3(1-2\nu)(z-\zeta)(x-\xi)}{R_1^5}+\frac{3(1-2\nu)(z-\zeta)(x-\xi)}{R_2^5}+\frac{6(z-\zeta)(x-\xi)}{R_1^5}-\frac{15(x-\xi)^3(z-\zeta)}{R_1^7}-\frac{15(3-4\nu)(x-\xi)^3(z-\zeta)}{R_2^7}\right.$$
$$+\frac{6(3-4\nu)(z-\zeta)(x-\xi)}{R_2^5}-\frac{8(1-2\nu)(1-\nu)(z-\zeta)(x-\xi)}{{R_2}^2(R_2+y+\eta)^3}-\frac{4(1-2\nu)(1-\nu)(z-\zeta)(x-\xi)}{{R_2}^3(R_2+y+\eta)^2}+\frac{12(1-2\nu)(1-\nu)(3R_2+y+\eta)(x-\xi)^3(z-\zeta)}{{R_2}^4(R_2+y+\eta)^4}$$
$$-\frac{12(1-2\nu)(1-\nu)(x-\xi)^3(z-\zeta)}{{R_2}^4(R_2+y+\eta)^3}-\frac{8(1-2\nu)(1-\nu)(3R_2+y+\eta)(z-\zeta)(x-\xi)}{{R_2}^3(R_2+y+\eta)^3}+\frac{12(1-2\nu)(1-\nu)(3R_2+y+\eta)(z-\zeta)^3(x-\xi)}{{R_2}^5(R_2+y+\eta)^3}$$
$$\left.-\frac{30y\eta(z-\zeta)(x-\xi)}{R_2^7}+\frac{210y\eta(x-\xi)^3(z-\zeta)}{R_2^9}-\frac{60\eta y(z-\zeta)(x-\xi)}{R_2^7}\right] \tag{A.9}$$

$$\frac{d\tau_{xz}^{R}}{d\eta}=\frac{1}{8\pi(1-\nu)}\left[\frac{3(z-\zeta)(x-\xi)}{R_1^5}-\frac{15(z-\zeta)(x-\xi)(y-\eta)^2}{R_1^7}+\frac{3(3-4\nu)(z-\zeta)(x-\xi)}{R_2^5}-\frac{15(3-4\nu)(z-\zeta)(x-\xi)(y-\eta)(y+\eta)}{R_2^7}\right.$$
$$+\frac{8(1-2\nu)(1-\nu)(z-\zeta)(x-\xi)(y+\eta)}{{R_2}^4(R_2+y+\eta)^2}+\frac{8(1-2\nu)(1-\nu)(z-\zeta)(x-\xi)\left(\frac{y+\eta}{R_2}+1\right)}{{R_2}^2(R_2+y+\eta)^3}+\frac{12(1-2\nu)(1-\nu)(z-\zeta)(x-\xi)(y+\eta)}{{R_2}^5(R_2+y+\eta)}$$
$$\left.+\frac{4(1-2\nu)(1-\nu)(z-\zeta)(x-\xi)\left(\frac{y+\eta}{R_2}+1\right)}{{R_2}^3(R_2+y+\eta)^2}+\frac{30\eta(z-\zeta)(x-\xi)(y+\eta)}{R_2^7}+\frac{30y\eta(z-\zeta)(x-\xi)}{R_2^7}-\frac{210y\eta(z-\zeta)(x-\xi)(y+\eta)^2}{R_2^9}\right] \tag{A.10}$$

$$\frac{d\tau_{xz}^{P}}{d\xi}=\frac{1}{8\pi(1-\nu)}\left[\frac{1-2\nu}{R_1^3}+\frac{3(1-2\nu)(x-\xi)^2}{R_1^5}-\frac{(1-2\nu)}{R_2^3}+\frac{3(1-2\nu)(x-\xi)^2}{R_2^5}+\frac{3(z-\zeta)^2}{R_1^5}-\frac{15(x-\xi)^2(z-\zeta)^2}{R_1^7}-\frac{15(3-4\nu)(x-\xi)^2(z-\zeta)^2}{R_2^7}+\frac{3(3-4\nu)(z-\zeta)^2}{R_2^5}\right.$$
$$+\frac{4(1-2\nu)(1-\nu)}{R_2(R_2+y+\eta)^2}-\frac{8(1-2\nu)(1-\nu)(x-\xi)^2}{R_2^2(R_2+y+\eta)^3}-\frac{4(1-2\nu)(1-\nu)(x-\xi)^2}{R_2^3(R_2+y+\eta)^2}+\frac{12(1-2\nu)(1-\nu)(3R_2+y+\eta)(x-\xi)^2(z-\zeta)^2}{R_2^4(R_2+y+\eta)^4}$$
$$-\frac{12(1-2\nu)(1-\nu)(x-\xi)^2(z-\zeta)^2}{R_2^4(R_2+y+\eta)^3}-\frac{4(1-2\nu)(1-\nu)(3R_2+y+\eta)(z-\zeta)^2}{R_2^3(R_2+y+\eta)^3}+\frac{12(1-2\nu)(1-\nu)(3R_2+y+\eta)(x-\xi)^2(z-\zeta)^2}{R_2^5(R_2+y+\eta)^3}+\frac{6y\eta}{R_2^5}-\frac{30y\eta(x-\xi)^2}{R_2^7}$$
$$\left.+\frac{210y\eta(x-\xi)^2(z-\zeta)^2}{R_2^9}-\frac{30y\eta(z-\zeta)^2}{R_2^7}\right] \tag{A.11}$$

$$\frac{d\tau_{xz}^{Q}}{d\zeta}=\frac{1}{8\pi(1-\nu)}\left[\frac{1-2\nu}{R_1^3}+\frac{3(1-2\nu)(z-\zeta)^2}{R_1^5}-\frac{(1-2\nu)}{R_2^3}+\frac{3(1-2\nu)(z-\zeta)^2}{R_2^5}+\frac{3(x-\xi)^2}{R_1^5}-\frac{15(x-\xi)^2(z-\zeta)^2}{R_1^7}-\frac{15(3-4\nu)(x-\xi)^2(z-\zeta)^2}{R_2^7}+\frac{3(3-4\nu)(x-\xi)^2}{R_2^5}\right.$$
$$+\frac{4(1-2\nu)(1-\nu)}{R_2(R_2+y+\eta)^2}-\frac{8(1-2\nu)(1-\nu)(z-\zeta)^2}{R_2^2(R_2+y+\eta)^3}-\frac{4(1-2\nu)(1-\nu)(z-\zeta)^2}{R_2^3(R_2+y+\eta)^2}+\frac{12(1-2\nu)(1-\nu)(3R_2+y+\eta)(x-\xi)^2(z-\zeta)^2}{R_2^4(R_2+y+\eta)^4}$$
$$-\frac{12(1-2\nu)(1-\nu)(x-\xi)^2(z-\zeta)^2}{R_2^4(R_2+y+\eta)^3}-\frac{4(1-2\nu)(1-\nu)(3R_2+y+\eta)(x-\xi)^2}{R_2^3(R_2+y+\eta)^3}+\frac{12(1-2\nu)(1-\nu)(3R_2+y+\eta)(x-\xi)^2(z-\zeta)^2}{R_2^5(R_2+y+\eta)^3}+\frac{6y\eta}{R_2^5}-\frac{30y\eta(z-\zeta)^2}{R_2^7}$$
$$\left.+\frac{210y\eta(x-\xi)^2(z-\zeta)^2}{R_2^9}-\frac{30y\eta(x-\xi)^2}{R_2^7}\right] \tag{A.12}$$

$$\frac{d\tau_{xz}^{P}}{d\eta}=\frac{1}{8\pi(1-\nu)}\left[-\frac{3(1-2\nu)(x-\xi)(y-\eta)}{R_1^5}+\frac{3(1-2\nu)(x-\xi)(y+\eta)}{R_2^5}-\frac{15(z-\zeta)^2(x-\xi)(y-\eta)}{R_1^7}-\frac{15(3-4\nu)(z-\zeta)^2(x-\xi)(y+\eta)}{R_2^7}\right.$$
$$-\frac{4(1-2\nu)(1-\nu)(x-\xi)(y+\eta)}{R_2^3(R_2+y+\eta)^2}-\frac{8(1-2\nu)(1-\nu)(x-\xi)\left(\frac{y+\eta}{R_2}+1\right)}{R_2(R_2+y+\eta)^2}-\frac{4(1-2\nu)(1-\nu)(z-\zeta)^2(x-\xi)\left(\frac{3(y+\eta)}{R_2}+1\right)}{R_2^3(R_2+y+\eta)^3}$$
$$+\frac{12(1-2\nu)(1-\nu)(z-\zeta)^2(x-\xi)(y+\eta)(3R_2+y+\eta)}{R_2^5(R_2+y+\eta)^3}+\frac{12(1-2\nu)(1-\nu)(z-\zeta)^2(x-\xi)(3R_2+y+\eta)\left(\frac{y+\eta}{R_2}+1\right)}{R_2^3(R_2+y+\eta)^4}-\frac{30y\eta(x-\xi)(y-\eta)}{R_2^7}+\frac{6\eta(x-\xi)}{R_2^5}$$
$$\left.-\frac{30\eta(z-\zeta)^2(x-\xi)}{R_2^7}+\frac{210y\eta(z-\zeta)^2(x-\xi)(y+\eta)}{R_2^9}\right] \tag{A.13}$$

$$\frac{d\tau_{xz}^{R}}{d\zeta}=\frac{1}{8\pi(1-\nu)}\left[\frac{3(x-\xi)(y-\eta)}{R_1^5}-\frac{15(z-\zeta)^2(x-\xi)(y-\eta)}{R_1^7}-\frac{15(3-4\nu)(z-\zeta)^2(x-\xi)(y-\eta)}{R_2^7}+\frac{3(3-4\nu)(x-\xi)(y-\eta)}{R_2^5}-\frac{4(1-2\nu)(1-\nu)(x-\xi)}{R_2^2(R_2+y+\eta)^2}\right.$$
$$+\frac{8(1-2\nu)(1-\nu)(z-\zeta)^2(x-\xi)}{R_2^4(R_2+y+\eta)^2}+\frac{8(1-2\nu)(1-\nu)(z-\zeta)^2(x-\xi)}{R_2^3(R_2+y+\eta)^3}-\frac{4(1-2\nu)(1-\nu)(x-\xi)}{R_2^3(R_2+y+\eta)}+\frac{4(1-2\nu)(1-\nu)(z-\zeta)^2(x-\xi)}{R_2^4(R_2+y+\eta)^2}$$
$$\left.+\frac{12(1-2\nu)(1-\nu)(z-\zeta)^2(x-\xi)}{R_2^5(R_2+y+\eta)}-\frac{210y\eta(z-\zeta)^2(x-\xi)(y+\eta)}{R_2^9}+\frac{30y\eta(x-\xi)(y+\eta)}{R_2^7}\right] \tag{A.14}$$

$$\frac{d\tau_{yz}^{P}}{d\zeta}=\frac{1}{8\pi(1-\nu)}\left[-\frac{3(1-2\nu)(z-\zeta)(y-\eta)}{R_1^5}+\frac{3(1-2\nu)(z-\zeta)(y-\eta)}{R_2^5}+\frac{6(z-\zeta)(y-\eta)}{R_1^5}-\frac{15(z-\zeta)^3(y-\eta)}{R_1^7}+\frac{6(3-4\nu)(z-\zeta)(y+\eta)}{R_2^5}\right.$$
$$\left.-\frac{15(3-4\nu)(z-\zeta)^3(y+\eta)}{R_2^7}-\frac{30y\eta(z-\zeta)(y+\eta)}{R_2^7}+\frac{30(1-2\nu)(z-\zeta)^3\eta}{R_2^7}-\frac{12(1-2\nu)\eta(z-\zeta)}{R_2^5}-\frac{60\eta y(z-\zeta)(y+\eta)}{R_2^7}+\frac{210y\eta(x-\xi)^3(z-\zeta)}{R_2^9}\right] \tag{A.15}$$

$$\frac{d\tau_{yz}^{Q}}{d\xi}=\frac{1}{8\pi(1-\nu)}\left[\frac{3(z-\zeta)(y-\eta)}{R_1^5}-\frac{15(z-\zeta)(x-\xi)^2(y-\eta)}{R_1^7}+\frac{3(3-4\nu)(z-\zeta)(y+\eta)}{R_2^5}-\frac{15(3-4\nu)(z-\zeta)(x-\xi)^2(y+\eta)}{R_2^7}+\frac{30(1-2\nu)\eta(z-\zeta)(x-\xi)^2}{R_2^7}\right.$$
$$\left.-\frac{6(1-2\nu)(z-\zeta)\eta}{R_2^5}-\frac{30y\eta(z-\zeta)(y+\eta)}{R_2^7}+\frac{210y\eta(z-\zeta)(x-\xi)^2(y+\eta)}{R_2^9}\right] \tag{A.16}$$

$$\frac{d\tau_{yz}^{R}}{d\eta}=\frac{1}{8\pi(1-\nu)}\left[-\frac{3(1-2\nu)(z-\zeta)(y-\eta)}{R_1^5}+\frac{3(1-2\nu)(z-\zeta)(y+\eta)}{R_2^5}+\frac{6(z-\zeta)(y-\eta)}{R_1^5}-\frac{15(y-\eta)^3(z-\zeta)}{R_1^7}-\frac{3(z-\zeta)[3\eta-(3-4\nu)(y+\eta)-(3-4\nu)y]}{R_2^5}+\frac{15(z-\zeta)(y+\eta)[\eta(3y+\eta)-(3-4\nu)(y+\eta)y]}{R_2^7}-\frac{210y\eta(y+\eta)^3(z-\zeta)}{R_2^9}+\frac{60\eta y(z-\zeta)(y+\eta)}{R_2^7}+\frac{30(z-\zeta)(y+\eta)^2\eta}{R_2^7}\right] \tag{A.17}$$

$$\frac{d\tau_{yz}^{P}}{d\xi}=\frac{1}{8\pi(1-\nu)}\left[-\frac{3(1-2\nu)(x-\xi)(y-\eta)}{R_1^5}+\frac{3(1-2\nu)(x-\xi)(y-\eta)}{R_2^5}-\frac{15(z-\zeta)^2(x-\xi)(y-\eta)}{R_1^7}-\frac{15(3-4\nu)(z-\zeta)^2(x-\xi)(y+\eta)}{R_2^7}-\frac{30y\eta(x-\xi)(y-\eta)}{R_2^7}+\frac{30(1-2\nu)\eta(z-\zeta)^2(x-\xi)}{R_2^7}+\frac{210y\eta(z-\zeta)^2(x-\xi)(y+\eta)}{R_2^9}\right] \tag{A.18}$$

$$\frac{d\tau_{yz}^{Q}}{d\zeta}=\frac{1}{8\pi(1-\nu)}\left[\frac{3(x-\xi)(y-\eta)}{R_1^5}-\frac{15(x-\xi)(z-\zeta)^2(y-\eta)}{R_1^7}+\frac{3(3-4\nu)(x-\xi)(y+\eta)}{R_2^5}-\frac{15(3-4\nu)(x-\xi)(z-\zeta)^2(y+\eta)}{R_2^7}+\frac{30(1-2\nu)\eta(x-\xi)(z-\zeta)^2}{R_2^7}-\frac{6(1-2\nu)(x-\xi)\eta}{R_2^5}-\frac{30y\eta(x-\xi)(y+\eta)}{R_2^7}+\frac{210y\eta(x-\xi)(z-\zeta)^2(y+\eta)}{R_2^9}\right] \tag{A.19}$$

$$\frac{d\tau_{yz}^{P}}{d\eta}=\frac{1}{8\pi(1-\nu)}\left[-\frac{3(1-2\nu)(y-\eta)^2}{R_1^5}+\frac{1-2\nu}{R_1^3}-\frac{1-2\nu}{R_2^3}+\frac{3(1-2\nu)(y-\eta)(y+\eta)}{R_2^5}+\frac{3(z-\zeta)^2}{R_1^5}-\frac{15(y-\eta)^2(z-\zeta)^2}{R_1^7}-\frac{15(3-4\nu)(y+\eta)^2(z-\zeta)^2}{R_2^7}+\frac{3(3-4\nu)(z-\zeta)^2}{R_2^5}+\frac{6\eta(y+\eta)}{R_2^5}+\frac{6y\eta}{R_2^5}-\frac{30y\eta(y+\eta)^2}{R_2^7}+\frac{30(1-2\nu)(z-\zeta)^2(y+\eta)\eta}{R_2^7}+\frac{210y\eta(y+\eta)^2(z-\zeta)^2}{R_2^9}-\frac{30y\eta(z-\zeta)^2}{R_2^7}-\frac{30\eta(z-\zeta)^2(y+\eta)}{R_2^7}\right] \tag{A.20}$$

$$\frac{d\tau_{yz}^{R}}{d\zeta}=\frac{1}{8\pi(1-\nu)}\left[-\frac{3(1-2\nu)(z-\zeta)^2}{R_1^5}+\frac{1-2\nu}{R_1^3}-\frac{1-2\nu}{R_2^3}+\frac{3(1-2\nu)(z-\zeta)^2}{R_2^5}+\frac{3(y-\eta)^2}{R_1^5}-\frac{15(y-\eta)^2(z-\zeta)^2}{R_1^7}+\frac{15(z-\zeta)^2[\eta(3y+\eta)-y(y+\eta)(3-4\nu)]}{R_2^7}-\frac{3\eta(3y+\eta)-3y(3-4\nu)(y+\eta)}{R_2^5}+\frac{30y\eta(y+\eta)^2}{R_2^7}-\frac{210y\eta(y+\eta)^2(z-\zeta)^2}{R_2^9}\right] \tag{A.21}$$

Where,

$$R_1=\sqrt{(x-\xi)^2+(y-\eta)^2+(z-\zeta)^2}$$

$$R_2=\sqrt{(x-\xi)^2+(y+\eta)^2+(z-\zeta)^2}$$

References

[1] Y. Yamashita, T. Murakami, R. Mihara, M. Okada, Y. Murakami, Defect analysis and fatigue design basis for Ni-based superalloy 718 manufactured by selective laser melting, Int. J. Fatigue 117 (2018) 485–495, https://doi.org/10.1016/j.ijfatigue.2018.08.002.

[2] R. Molaei, A. Fatemi, Crack paths in additive manufactured metallic materials subjected to multiaxial cyclic loads including surface roughness, HIP, and notch effects, Int. J. Fatigue 124 (2019) 558–570, https://doi.org/10.1016/j.ijfatigue.2019.03.007.

[3] M. Madia, B. Schork, J. Bernhard, M. Kaffenberger, Multiple crack initiation and propagation in weldments under fatigue loading, Procedia Struct Integr 7 (2017) 423–430, https://doi.org/10.1016/j.prostr.2017.11.108.

[4] M. Åman, K. Wada, H. Matsunaga, H. Remes, G. Marquis, The influence of interacting small defects on the fatigue limits of a pure iron and a bearing steel, Int. J. Fatigue 135 (2020), 105560, https://doi.org/10.1016/j.ijfatigue.2020.105560.

[5] M. Åman, S. Okasaki, H. Matsunaga, G.B. Marquis, H. Remes, Interaction effect of adjacent small defects on the fatigue limit of a medium carbon steel, Fatigue Fract. Eng. Mater. Struct. 40 (2017) 130–144, https://doi.org/10.1111/ffe.12482.

[6] A. Abass, K. Wada, H. Matsunaga, H. Remes, T. Vuorio, Quantitative Characterization of the Spatial Distribution of Corrosion Pits Based on Nearest Neighbor Analysis, Corrosion 76 (9) (2020) 861–870, https://doi.org/10.5006/3551.

[7] T. Winkler, A. Bruckner-Foit, H. Riesch-Oppermann, Statistical characterisation of random crack patterns caused by thermal fatigue, Fatigue Fract. Eng. Mater. Struct. 15 (10) (2007) 1025–1039, https://doi.org/10.1111/j.1460-2695.1992.tb00029.x.

[8] H. Kitagawa, T. Fujita, K. Miyazawa, Small Randomly Distributed Cracks in Corrosion Fatigue, ASTM International STP28716S (1978) 98–114, https://doi.org/10.1520/STP28716S.

[9] S. Romano, S. Miccoli, S. Beretta, A new FE post-processor for probabilistic fatigue assessment in the presence of defects and its application to AM parts, Int. J. Fatigue 125 (2019) 324–341, https://doi.org/10.1016/j.ijfatigue.2019.04.008.

[10] R.N. Parkins, E. Belhimer, W.K. Blanchard Jr, Stress Corrosion Cracking Characteristics of a Range of Pipeline Steels in Carbonate-Bicarbonate Solution, Corrosion 49 (12) (1993) 951–966, https://doi.org/10.5006/1.3316023.

[11] S. Beretta, Y. Murakami, Statistical Analysis of Defects for Fatigue Strength Prediction and Quality Control of Materials, Fatigue Fract. Eng. Mater. Struct. 21 (9) (1998) 1049–1065, https://doi.org/10.1046/j.1460-2695.1998.00104.x.

[12] O. Partl, J. Schijve, Multiple-site damage in 2024–T3 alloy sheet, Int. J. Fatigue 15 (4) (1993) 293–299, https://doi.org/10.1016/0142-1123(93)90378-4.

[13] J.R. Cahoon, H.W. Paxton, Metallurgical analyses of failed orthopedic implants, J. Biomed. Mater. Res. 2 (1968) 1–22, https://doi.org/10.1002/jbm.820020102.

[14] Y.Z. Wang, J.D. Atkinson, R. Akid, R.N. Parkins, Crack Interaction, Coalescence and Mixed Mode Fracture Mechanics, Fatigue Fract. Eng. Mater. Struct. 19 (4) (1996) 427–439, https://doi.org/10.1111/j.1460-2695.1996.tb00979.x.

[15] V.V. Panasyuk, A.E. Andreikiv, M.M. Stadnik, Three-dimensional static crack problems solution (a review), Eng. Fract. Mech. 14 (2) (1981) 245–260, https://doi.org/10.1016/0013-7944(81)90001-1.

[16] M. Isida, H. Tsuru, H. Noguchi, An Analysis for Three Dimensional Cracks, Fatigue Fract. Eng. Mater. Struct. 17 (7) (1994) 737–749, https://doi.org/10.1111/j.1460-2695.1994.tb00805.x.

[17] J. Weaver, Three-dimensional crack analysis, Int. J. Solids Struct. 13 (4) (1977) 321–330, https://doi.org/10.1016/0020-7683(77)90016-6.

[18] M.K. Kassir, G.C. Sih, Three-Dimensional Stress Distribution Around an Elliptical Crack Under Arbitrary Loadings, J. Appl. Mech. 33 (3) (1966) 601–611, https://doi.org/10.1115/1.3625127.

[19] M. Isida, A. Tokumoto, H. Noguchi, Oblique semi-elliptical surface crack in semi-infinite solid subjected to tension, Eng. Fract. Mech. 36 (6) (1990) 889–892, https://doi.org/10.1016/0013-7944(90)90265-I.
[20] Y. Murakami, M. Isida, Analysis of Mixed Mode Stress Intensity Factors for Arbitrarily Shaped Inclined Surface Cracks, Trans Japan Soc Mech Eng A 50 (455) (1984) 1359–1366, https://doi.org/10.1299/kikaia.50.1359.
[21] Y. Murakami, Analysis of stress intensity factors of modes I, II and III for inclined surface cracks of arbitrary shape, Eng. Fract. Mech. 22 (1) (1985) 101–114, https://doi.org/10.1016/0013-7944(85)90163-8.
[22] M. Isida, H. Noguchi, T. Yoshida, Tension and bending of finite thickness plates with a semi-elliptical surface crack, Int. J. Fract. 26 (1984) 157–188, https://doi.org/10.1007/BF01140626.
[23] J.P. Benthem, State of stress at the vertex of a quarter-infinite crack in a half-space, Int. J. Solids Struct. 13 (5) (1977) 479–492, https://doi.org/10.1016/0020-7683(77)90042-7.
[24] Y. Murakami, H. Natsume, Stress Singularity at the Corner Point of 3-D Surface Crack under Mode II Loading, JSME Int J A-Solid M 45 (2) (2002) 161–169, https://doi.org/10.1299/jsmea.45.161.
[25] N.A. Noda, T. Kihara, D. Beppu, Variations of stress intensity factor of a semi-elliptical surface crack subjected to mixed mode loading, Int. J. Fract. 127 (2004) 167–191, https://doi.org/10.1023/B:FRAC.0000035054.88722.43.
[26] M.Y. He, J.W. Hutchinson, Surface crack subject to mixed mode loading, Eng. Fract. Mech. 65 (1) (2000) 1–14, https://doi.org/10.1016/S0013-7944(99)00129-0.
[27] L.P. Pook, F. Berto, A. Campagnolo, State of the art of corner point singularities under in-plane and out-of-plane loading, Eng. Fract. Mech. 174 (2017) 2–9, https://doi.org/10.1016/j.engfracmech.2016.10.001.
[28] N.A. Noda, S. Miyoshi, Variation of stress intensity factor and crack opening displacement of semi-elliptical surface crack, Int. J. Fract. 75 (1996) 19–48, https://doi.org/10.1007/BF00018524.
[29] C. Ruiz, J. Epstein, On the variation of the stress intensity factor along the front of a surface flaw, Int. J. Fract. 28 (1985) 231–238, https://doi.org/10.1007/BF00035218.
[30] S.K. Chan, I.S. Tuba, W.K. Wilson, On the finite element method in linear fracture mechanics, Eng. Fract. Mech. 2 (1) (1970) 1–17, https://doi.org/10.1016/0013-7944(70)90026-3.
[31] M. Kachanov, J.P. Laures, Three-dimensional problems of strongly interacting arbitrarily located penny-shaped cracks, Int. J. Fract. 41 (1989) 289–313, https://doi.org/10.1007/BF00018861.
[32] V.I. Fabrikant, Close interaction of coplanar circular cracks under shear loading, Comput. Mech. 4 (1989) 181–197, https://doi.org/10.1007/BF00296666.
[33] S. Zhan, T. Wang, Interactions of Penny-shaped Cracks in Three-dimensional Solids, Acta Mech. Solida Sin. 22 (2006) 341–353, https://doi.org/10.1007/s10409-006-0007-8.
[34] P.E. O'Donoghue, T. Nishioka, S.N. Atluri, Multiple coplanar embedded elliptical cracks in an infinite solid subject to arbitrary crack face tractions, Int. J. Numer. Meth. Eng. 21 (3) (1985) 437–449, https://doi.org/10.1002/nme.1620210305.
[35] M.A. Hasib, Y. Sonobe, A. Saimoto, Improvement of Stress Intensity Factor Analysis Using Overall Defined Basic Density Function on Crack Face, J. Multiscale Model. 9 (1) (2018) 1750006, https://doi.org/10.1142/S1756973717500068.
[36] M. Kachanov, Elastic solids with many cracks: A simple method of analysis, Int. J. Solids Struct. 23 (1) (1987) 23–43, https://doi.org/10.1016/0020-7683(87)90030-8.
[37] H. Horii, S. Nemat-Nasser, Elastic fields of interacting inhomogeneities, Int. J. Solids Struct. 21 (7) (1985) 731–745, https://doi.org/10.1016/0020-7683(85)90076-9.
[38] Y. Murakami, S. Nemat-Nasser, Interacting dissimilar semi-elliptical surface flaws under tension and bending, Eng. Fract. Mech. 16 (3) (1982) 373–386, https://doi.org/10.1016/0013-7944(82)90115-1.
[39] Y. Murakami, S. Nemat-Nasser, Growth and stability of interacting surface flaws of arbitrary shape, Eng. Fract. Mech. 17 (3) (1983) 193–210, https://doi.org/10.1016/0013-7944(83)90027-9.
[40] M. Isida, T. Yoshida, H. Noguchi, Parallel array of semi-elliptical surface cracks in semi-infinite solid under tension, Eng. Fract. Mech. 39 (5) (1991) 845–850.
[41] W.A. Moussa, R. Bell, C.L. Tan, The interaction of two parallel non-coplanar identical surface cracks under tension and bending, Int. J. Press. Vessels Pip. 76 (3) (1999) 135–145, https://doi.org/10.1016/S0308-0161(98)00125-2.
[42] M. Åman, K. Berntsson, G. Marquis, An efficient stress intensity factor evaluation method for interacting arbitrary shaped 3D cracks, Theor. Appl. Fract. Mech. 109 (2020), 102767, https://doi.org/10.1016/j.tafmec.2020.102767.
[43] B.A. Bilby, A.H. Cottrell, K.H. Swinden, The spread of plastic yield from a notch, Proc. R. Soc. Lond. A 272 (1350) (1963) 304–314, https://doi.org/10.1098/rspa.1963.0055.
[44] D.A. Hills, P.A. Kelly, D.N. Dai, A.M. Korsunsky, Solution of Crack Problems: The Distributed Dislocation Technique, 1st ed, Springer Dordrecht, Netherlands, 1996. https://doi.org/10.1007/978-94-015-8648-1.
[45] Z.P. Bažant, L.F. Estenssoro, Surface singularity and crack propagation, Int. J. Solids Struct. 15 (5) (1979) 405–426, https://doi.org/10.1016/0020-7683(79)90062-3.
[46] J.P. Benthem, The quarter-infinite crack in a half space; Alternative and additional solutions, Int. J. Solids Struct. 16 (2) (1980) 119–130, https://doi.org/10.1016/0020-7683(80)90029-3.
[47] J. Hadamard, Lectures on Cauchy's Problem in Linear Partial Differential Equations, Dover Publications Inc, New York, 1952.
[48] T. Mura, Micromechanics of Defects in Solids, 1st ed., Martinus Nijhoff Publishers, The Hague, 1982 https://doi.org/10.1007/978-94-011-9306-1.
[49] D.J. Bacon, P.P. Groves, The Dislocation in a Semi-Infinite Isotropic Medium. In: Simmons JA, de Witt R, Bullough R, editors. Fundamental Aspects of Dislocation Theory, Washington DC: National Bureau of Standards Special Publication 317, vol. I; 1970, p. 35-45.
[50] R.D. Mindlin, Force at a point in the interior of a semi-infinite solid, Physics 7 (1936) 195–202.
[51] Y. Murakami, K. Takahashi, T. Yamashita, Quantitative Evaluation of the Effect of Surface Roughness on Fatigue Strength: Effect of Depth and Pitch of Roughness, Trans Jpn Soc Mech Eng A 63 (612) (1997) 1612–1619, https://doi.org/10.1299/kikaia.63.1612.
[52] S. Okazaki, S. Okuma, Ogawa Y. Kevinsanny, H. Kawashima, Y. Funakoshi, H. Matsunaga, Unforeseen, negative interaction-effect of adjacent circumferential notches on the fatigue limit of Ni-based superalloy 718, Eng. Fract. Mech. 257 (2021) 108015, https://doi.org/10.1016/j.engfracmech.2021.108015.
[53] ISO 4967:2013, Steel – Determination of content of non-metallic inclusions – Micrographic method using standard diagrams. International Organization for Standardization.
[54] JIS G 0555:2003, Microscopic testing method for the non-metallic inclusions in steel. Japanese Standards Association.
[55] ASTM E45-13, Standard Test Methods for Determining the Inclusion Content of Steel. ASTM International (American Section of the International Association for Testing Materials).
[56] Y. Murakami, Metal Fatigue: Effects of Small Defects and Nonmetallic Inclusions, 1st ed., Elsevier Science, Oxford, 2002.
[57] G. Wranglen, Pitting and sulphide inclusions in steel, Corros. Sci. 14 (5) (1974) 331–349, https://doi.org/10.1016/S0010-938X(74)80047-8.
[58] A. Boukerrou, R.A. Cottis, Crack initiation in the corrosion fatigue of structural steels in salt solutions, Corros. Sci. 35 (1–4) (1993) 577–585, https://doi.org/10.1016/0010-938X(93)90192-J.